

1 **Increasing precipitation due to climate change could partially**
2 **offset the impact of warming on glacier loss in the monsoon-**
3 **influenced Himalaya until 2100 CE**

4
5 Anya M. Schlich-Davies^{1*}, Ann V. Rowan^{2*}, Andrew N. Ross¹, Duncan J. Quincey³, Vivi K.
6 Pedersen⁴

7
8 ¹Priestley International Centre for Climate, School of Earth and Environment, University of Leeds,
9 UK

10 ²Department of Earth Science, University of Bergen and Bjerknes Centre for Climate Research,
11 Bergen, Norway

12 ³School of Geography, University of Leeds, UK

13 ⁴Department of Geoscience, Aarhus University, Aarhus C, Denmark

14
15 *These authors contributed equally to this work

16
17 Correspondence to: Ann V. Rowan (ann.rowan@uib.no)

18
19
20 **Abstract.** Glacier mass in the Himalaya is projected to shrink by 53–70% due to climate change by
21 2100 CE. However, the impact of changes in precipitation amount and distribution on future glacier
22 change remains uncertain because **this variable** is not **often** represented in **glacier model projections**.
23 We explored the combined effects of past and future changes in air temperature and precipitation
24 amount and distribution on the evolution of Khumbu Glacier in the Everest region of Nepal. We used a
25 glacier modelling approach that forced an ice-dynamical glacier evolution model with surface mass
26 balance **calculations** that included mesoscale meteorological variables derived from **statistical**
27 downscaling of **existing regional climate projections**. Our simulations show that historical warming has
28 committed Khumbu Glacier to mass loss of 10–23% during this century, and that under an intermediate
29 future emissions scenario (RCP4.5), **this glacier** could lose 70% mass by 2100 CE due to warming. **The**
30 projected increase in precipitation in tandem with warming could offset about half of the projected
31 glacier loss, such that the total decrease in glacier mass by 2100 CE compared to the present day would
32 be reduced to 34%. **However, under a higher** future emissions scenario (RCP8.5) glacier loss due to
33 warming will not be compensated by changes in precipitation, but will instead result in substantial
34 ablation above 6,000 m **elevation**, with devastating consequences for one of the highest glaciers on
35 Earth.

36
37 **1. Introduction**

38 Projecting glacier change in response to climate change is important for determining the impact of
39 anthropogenic warming on regional water availability (Pritchard, 2019). High Mountain Asia is
40 projected to lose 34 ± 19% of glacier mass by 2100 CE if warming is limited to 1.5°C to meet the
41 ambitious Paris Agreement target (Kraaijenbrink et al., 2017). Less ambitious projections give 53 ±
42 23% glacier mass loss by 2100 CE under the intermediate emissions scenario RCP4.5, and 69 ± 20%
43 under the high emissions scenario RCP8.5 (Kraaijenbrink et al., 2017; Marzeion et al., 2020; Rounce
44 et al., 2023). **Such projections are challenging to make, because accumulation and ablation processes**
45 **in mountain environments are driven by orographic feedbacks between high-relief topography and**
46 **atmospheric circulation systems such as the South Asian Summer Monsoon (e.g., Bookhagen and**
47 **Burbank, 2006). Furthermore, large uncertainties arise from the challenge of simulating the interactions**
48 **between the mass balance regimes of monsoon-influenced glaciers, where accumulation and ablation**
49 **both occur during the monsoon season, and the dynamics of glaciers flowing through high-relief**
50 **topography that includes processes such as the development of supraglacial debris layers that modify**
51 **surface melting (Dehecq et al., 2019; Miles et al., 2018b; Salerno et al., 2023). Variability in the extent**
52 **and intensity of the Indian Summer Monsoon during the Last Glacial Maximum was shown to affect**
53 **glacier expansion in the monsoon-influenced Himalaya through changes in snowfall distribution (Benn**

Deleted: mesoscale meteorology

Deleted: current

Deleted: s

Deleted: climate-

Deleted: forcings

Deleted: Regional Climate Model results

Deleted:

Deleted: future

Deleted: Khumbu Glaci

Deleted: However,

Deleted: t

Deleted: U

Deleted: mass

Deleted: However,

Deleted: s

Deleted: ted

70 and Owen, 1998; Owen et al., 2009). Future Indian Summer Monsoon precipitation and variability
71 projected in Global Circulation Models (GCMs) will increase with current global warming
72 (Katzenberger et al., 2021), but as yet, the effect of projected changes in precipitation amount, timing,
73 and phase (rain/snow) on Himalayan glaciers remain poorly constrained (Immerzeel et al., 2012; Mölg
74 et al., 2014; Ragetti et al., 2016; Shaw et al., 2022; Shea et al., 2015).

75
76 Supraglacial debris covers 4–7% of glacier surfaces globally and 30% of glacier ablation areas in the
77 Himalaya, and modifies the response of glaciers to climate change relative to regional trends (Herreid
78 and Pellicciotti, 2020; Kraaijenbrink et al., 2017; Rounce et al., 2023; Rowan et al., 2015). Satellite
79 observations show that the rate of glacier mass loss across the Himalaya has accelerated over the last
80 40 years for both clean-ice glaciers and debris-covered glaciers (Maurer et al., 2019). Observations and
81 modelling studies indicate that thick supraglacial debris caused historical mass loss from debris-covered
82 glaciers to lag that of clean-ice glaciers, such that debris-covered glaciers are currently larger than would
83 otherwise be the case (King et al., 2020; Rounce et al., 2023; Rowan et al., 2021). However, the
84 dampening effect of supraglacial debris on glacier mass loss is overturned by the development of
85 extensive supraglacial ponds and ice cliffs within debris layers (Miles et al., 2018a; Strickland et al.,
86 2023) and the stagnation and detachment of debris-covered tongues from the upper and more active
87 sections of these glaciers (Rowan et al., 2021). Quantifying the impact of feedbacks set up by the
88 formation and expansion of supraglacial debris layers at a regional scale requires exploring such
89 processes at scales that can be resolved in ice-dynamical glacier evolution models (Rowan et al., 2015;
90 Nicholson et al., 2021; Compagno et al., 2022). These processes can be considered in 2-D (along the
91 glacier flowline) either considering stochastic debris delivery to the glacier (Vacca et al., 2010) or
92 continuous debris delivery, which can result in the over-accumulation of debris at the terminus
93 (Anderson and Anderson, 2016; Ferguson and Vieli, 2020; Jouviet et al., 2011), or in 3-D (using the
94 horizontal and vertical ice-flow fields), which simulates the lateral transport and deposition of debris to
95 the margins of the ablation area (Rowan et al., 2015; Wirbel et al., 2018).

96
97 While recent rapid warming has resulted in a rise in regional equilibrium line altitude (ELA) and caused
98 recession and collapse of glacier termini for both clean-ice glaciers and debris-covered glaciers (King
99 et al., 2020), the decay of the former ablation areas of debris-covered glaciers is delayed by supraglacial
100 debris, such that the terminus of the actively flowing glacier can remain in contact with the detached
101 ice tongue rather than separating (Maurer et al., 2019; Pellicciotti et al., 2015; Rowan et al., 2021). In
102 common with most large debris-covered Himalayan glaciers, Khumbu Glacier in the Everest region of
103 Nepal (Fig. 1) is in greater imbalance with climate than a climatically equivalent clean-ice glacier, and
104 has maintained a more extensive ice volume than would be possible without supraglacial debris (Rowan
105 et al., 2021). However, as a result of reduced ice flux from the accumulation area, the debris-covered
106 tongue no longer receives much (or any) input of ice, and has dynamically detached from the active
107 glacier (Fig. 1C); this observation is confirmed by the rapid reduction in ice flow and the peak in glacier
108 surface lowering below the Khumbu Icefall where the debris layer is thinnest (King et al., 2020;
109 Quincey et al., 2009). Therefore, the active glacier and the stagnant debris-covered tongue will evolve
110 along different trajectories, and only the part of Khumbu Glacier above the terminus of the active glacier
111 can be considered dynamic (Miles et al., 2022). Projections of future glacier evolution should therefore
112 discount the heavily debris-covered former tongue, which is decaying *in situ* without any input of new
113 ice from the accumulation area, while considering the development of supraglacial debris across the
114 ablation area of the active glacier.

115
116 We applied a novel glacier modelling approach to Khumbu Glacier to test the hypothesis that changes
117 in precipitation in response to climate change will reduce the impact of warming on glacier mass loss.
118 Khumbu Glacier is a benchmark debris-covered glacier in the monsoon-influenced Himalaya flowing
119 from 7,981 m above sea level (a.s.l.) to 4,879 m a.s.l. that is representative in terms of elevation of the
120 majority of glaciers in the Central and Eastern Himalaya (Fig. 1B). We used a 3-D ice-flow model
121 forced by mass balance calculated from mesoscale meteorological variables to simulate the evolution
122 of Khumbu Glacier from the late Holocene (~1 ka) through the present day (2015 CE) until 2100 CE
123 using results from three downscaled Regional Climate Models (RCMs) under two Relative
124 Concentration Pathways (RCPs). This approach represents an advance in the use of such models to

Deleted: these

Deleted: ; Wirbel et al., 2018

Deleted:

Deleted: allows

Deleted: , that

Deleted: relatively

Deleted: c

Deleted: (Fig. 1).

Deleted: -climate

Deleted: this region

135 understand the evolution of Himalayan glaciers whereby mesoscale meteorological forcing of surface
136 mass balance is used with a thermomechanical glacier model to represent the processes of sublimation,
137 snow avalanching, and debris transport, all of which are important controls on the mass balance of
138 Himalayan glaciers (Kneib et al., 2025). Simulations start from the late Holocene when Khumbu Glacier
139 was last in dynamic equilibrium with the local climate, as evidenced by large ice-marginal moraines
140 dated to 1.3 ± 0.1 ka surrounding the present-day glacier (Hornsey et al., 2022), and when the glacier
141 surface was free of debris (Rowan et al., 2015).

142
143 Khumbu Glacier (RGI2000-v7.0-G-15-08331) is 16.0 km long with an area of 26.4 km². The median
144 glacier elevation is 6,025 m a.s.l. from the terminus at 4,879 m a.s.l. to the headwall at 7,981 m a.s.l.
145 (RGI 7.0 Consortium, 2023). The stagnant debris-covered tongue has an area of 6.2 km² (23% of the
146 total glacier). The 'Little Ice Age' (LIA) maximum of Khumbu Glacier occurred about 200–500 years
147 before present, which is consistent with ages produced for moraines elsewhere in the central Himalaya
148 (Hornsey et al., 2022; Rowan, 2017). Khumbu Glacier was slightly larger than today during the late
149 Holocene, transitioning from a clean-ice glacier with high velocities and efficient export of debris to a
150 debris-covered glacier with lower velocities after the LIA; this change was initiated by the reduction in
151 ice flux to the glacier tongue promoted by a rise in ELA (Rowan et al., 2015). Observations and
152 modelling of the dynamics and structure of Khumbu Glacier show that the tongue for 5 km upglacier
153 from the terminus (25% of the total length, 20% of total ice volume) is stagnant and dynamically
154 detached from the active glacier in the last century (Miles et al., 2022; Quincey et al., 2009; Rowan et
155 al., 2021). Basal ice at the glacier surface indicates that the active terminus overrides the stagnant glacier
156 tongue (Miles et al., 2021) and measurements of surface displacement show no longitudinal flow
157 through the detached debris-covered tongue, which is collapsing laterally at a rate of about 3 m a⁻¹
158 (Watson et al., 2017).

159 2. Methods

160 2.1 Glacier model experimental design

161 The glacier model experiments used mesoscale meteorological variables to calculate surface mass
162 balance for the Khumbu Glacier catchment in combination with a debris-covered glacier evolution
163 model to represent the surface processes that modify mass balance (Fig. 2A). Our approach produced a
164 total of six simulations of Khumbu Glacier to 2100 CE from three CORDEX South Asia region RCMs
165 (NOAA, CCCma, IPSL; Lutz et al., 2016) under two RCPs (RCP4.5 and RCP8.5; Collins et al., 2013)
166 to explore the impacts of possible variability in future precipitation amount and distribution in tandem
167 with warming on glacier evolution. Before we used the RCMs to force the future climate scenarios, we
168 evaluated their capabilities against observations of present-day weather and climate. The experimental
169 design represents an advance compared with previous glacier modelling efforts by including in each
170 simulation: (1) mesoscale meteorological phenomena, including sublimation, (2) the redistribution of
171 surface mass by snow avalanching, and (3) the feedbacks between debris transport, ice flow and mass
172 balance. This section describes the experimental design for the glacier modelling workflow,
173 downscaling of the present-day RCMs using meteorological data from automatic weather stations
174 (AWS) in the Khumbu Valley, downscaling of the future RCMs for both RCPs, the surface energy and
175 mass balance calculations using COSIPY (Sauter et al., 2020) and the debris-covered glacier evolution
176 modelling using iSOSIA (Rowan et al., 2015). A reference simulation and sensitivity experiments were
177 carried out for the period 2013–2015 CE, and the simulations of future glacier change represented the
178 period 2015–2100 CE. Additional information about the development and testing of the modelling
179 approach is provided in Appendix A.

180
181
182 The ice-free model domain was found by subtracting the estimated ice thickness (Farinotti et al., 2019)
183 from a 30-m digital elevation model (DEM) acquired from the Shuttle Radar Topography Mission (Farr
184 et al., 2007). The ice-free model domain incorporated the full hydrological catchment including the
185 steep hillslopes in the Western Cwm that provide snow to the glacier surface by avalanching. As a
186 starting point for our transient simulations of Khumbu Glacier, we reconstructed the late Holocene
187 glacier from an ice-free domain using an ELA of 5,325 m a.s.l. and an atmospheric lapse rate of -4.0°C
188 km^{-1} in a 5,000 year simulation. This simulation continued through the LIA forced by a step change in
189 mean annual air temperature (MAAT) equivalent to 1.5°C colder than the present day over 500 years

Deleted: ; for the first time

Deleted: climate

Deleted: -glacier

Deleted: hat

Deleted: s

Deleted: The focus of our experiments is to simulate glacier evolution to the end of the 21st Century. However, the centennial dynamic response time of a large debris-covered glacier such as Khumbu Glacier means that the glacier continues to evolve beyond this time scale, and we continued the simulations until 2300 CE to explore longer-term glacier evolution, albeit with greater uncertainties associated with results beyond 2100 CE.

Moved (insertion) [1]

Deleted: 2. Climate-glacier modelling of Khumbu Glacier

Deleted: n

Deleted: during

Deleted: ;

Deleted: and thickening supraglacial debris

Deleted: lowest five

Deleted: 1

Deleted: ¶

Moved up [1]: Khumbu Glacier (RGI2000-v7.0-G-15-08331) is 16.0 km long with an area of 26.4 km². The median glacier elevation is 6,025 m a.s.l. from the terminus at 4,879 m a.s.l. to the headwall at 7,981 m a.s.l. (RGI 7.0 Consortium, 2023). The stagnant debris-covered tongue has an area of 6.2 km² (23% of the total glacier). The 'Little Ice Age' (LIA) maximum of Khumbu Glacier occurred about 500 years before present, which is consistent with ages produced for moraines elsewhere in the central Himalaya (Hornsey et al., 2022; Rowan, 2017). Khumbu Glacier was slightly larger than today during the late Holocene, transitioning from a clean-ice glacier with high velocities and efficient export of debris to a debris-covered glacier with lower velocities during the LIA; this change was initiated by the reduction in ice flux promoted by a rise in ELA and thickening supraglacial debris (Rowan et al., 2015). Observations and modelling of the dynamics and structure of Khumbu Glacier show that the lowest five km (25% of the total length, 20% of total ice volume) is stagnant and dynamically detached from the active glacier in the last century (Miles et al., 2021; Quincey et al., 2009; Rowan et al., 2021). Basal ice at the glacier surface indicates that the active terminus overrides the stagnant glacier tongue (Miles et al., 2021) and measurements of surface displacement show no longitudinal flow through

Deleted: The climate-glacier glacier model experiments used mesoscale meteorological variables at an appropriate sc... [1]

Formatted: Normal, Left

Deleted: -climate

Deleted: As a starting point for our transient simulations of Khumbu Glacier, we reconstructed the late Holocene gl... [2]

Formatted: Normal

Deleted: We simulated only the active section of the glacier to the present day and future, and assigned the detached... [3]

312 following the approach of Rowan et al. (2015, 2021). Ice-marginal moraines denoting the late Holocene
 313 (1.3 ± 0.1 ka) glacier extent and thickness (Hornsey et al., 2022) were used to constrain the spin-up
 314 simulation. The late Holocene simulation was forced to present-day conditions using three surface mass
 315 balances (one from each RCM) calculated using the Coupled Snowpack and Ice-surface Energy and
 316 Mass Balance model in Python (COSIPY v1.3) (Sauter et al., 2020). These simulations were evaluated
 317 against a range of observations of present-day glaciology and previous glacier model experiments (Fig.
 318 3), and the experiment using the NOAA RCM was identified as the starting point for all future
 319 simulations because this was most representative of the observed glacier. We simulated only the active
 320 section of the glacier and assigned the dynamically detached debris-covered tongue to the model domain
 321 as a static topographic feature by using the simulated present-day velocity field to separate the simulated
 322 ice volume. Thus, we arrived at the present-day from the LIA maximum simulation by forcing the LIA
 323 glacier with the 2015–2020 CE mass balance for 200 years. We used the output from the present-day
 324 simulation with the 2095–2100 CE mass balance to force the model to 2100 CE for a period of 80 years.
 325 The glacier model simulations continued from the present day to 2100 CE forced by distributed glacier
 326 surface mass balances calculated for each of the three RCMs and two RCPs using COSIPY. The three
 327 RCMs and two future RCPs represented a range of possible future climates with distinctly different
 328 precipitation trends—equivalent to dry, moderate, and wet scenarios for warming of 1.4–2.2°C under
 329 RCP4.5 and 3.8–4.1°C under RCP8.5 (Table 1; Section 2.3). We used time slices representing the
 330 present day (2015–2020 CE) and the end of the 21st Century (2095–2100 CE) to calculate surface mass
 331 balance, and the preceding decade was used to evaluate these time slices (see Section 3.3). We used this
 332 step forcing, whereby the future mass balance was imposed and the glacier adjusted to this from the
 333 start of the century in question, rather than interpolating mass balance over time to reduce the
 334 computational expense of the surface mass balance and glacier modelling (~24 hours per simulation).

335 We tested a range of lapse rates from $-3.0^{\circ}\text{C km}^{-1}$ to $-6.0^{\circ}\text{C km}^{-1}$ while maintaining the same ELA
 336 based on the range of monthly values calculated from regression of NASA MODIS land surface
 337 temperature data for the Central Himalaya, which resulted in a difference in ice volume of $0.4 \times 10^9 \text{ m}^3$
 338 and no change in glacier length at the present day (result not shown). Estimates from a global glacier
 339 modelling study indicate that avalanching contributes up to 18% of regional accumulation to glaciers
 340 in the monsoon-influenced Himalaya (Kneib et al., 2025) and observations of high-elevation Himalayan
 341 glaciers, including Khumbu Glacier, suggest that up to 75% of accumulation occurs by avalanching
 342 rather than direct snowfall (Fig. 1D) (Benn and Lehmkuhl, 2000; Laha et al., 2017). Avalanching affects
 343 mountain glaciers in two ways: (1) by moving snow from steep hillslopes onto the glacier surface thus
 344 increasing accumulation from that calculated from direct snowfall onto the glacier surface, and (2) by
 345 redistributing snow across steep sections of the glacier surface (Kneib et al., 2025). We examined the
 346 uncertainty in accumulation resulting from the application of a calculation to move snowfall from slopes
 347 susceptible to avalanching (see Section 2.6). If avalanching was not considered in jSOSIA, then the
 348 accumulation of snow calculated using COSIPY within the catchment but outside of the glacier outline
 349 would have no impact on accumulation, resulting in an underestimation of ice volume, and the steep
 350 sections of the glacier would hold more mass than expected. For example, when avalanching was not
 351 simulated and accumulation occurred at a uniform rate of $2.0 \text{ w.e. m a}^{-1}$ across the Western Cwm
 352 accumulation area, Khumbu Glacier had a similar extent but a volume more than double that of the
 353 glacier simulated with avalanche redistribution of snow, because mass was not redistributed effectively
 354 across steep sections of the glacier surface (result not shown).

2.2 Meteorological data collection and analysis

358 The first meteorological observations for the Nepal Himalaya were collected during the 1970s and
 359 found a trend of diurnal precipitation on ridges and nocturnal precipitation in valley floors (Ageta, 1976)
 360 reflecting cloud development from orographic convection during the day. Continuously recording AWS
 361 were first installed in the region in the 1990s at the Pyramid Observatory near Lobuche village, where
 362 Bollasina et al. (2002) analysed of the monsoon from meteorological observations collected between
 363 1994 and 1999, finding that the onset (decay) of the Indian Summer Monsoon was distinguished by
 364 higher (lower) daily precipitation totals, mean relative humidity and atmospheric pressure and a reduced
 365 (increased) diurnal range in atmospheric temperature. Bollasina et al. (2002) identified two daily
 366 profiles in precipitation and wind direction thought to be related to the monsoon. In addition, five-day

Deleted: spin-up

Deleted: For more detail on the glacier model parameterisation and evaluation of the present-day simulation using geological and remote sensing observations, we refer to Rowan et al. (2021). ¶

Deleted: the

Deleted: including

Deleted: ,

Deleted: under

Deleted: 2

Deleted: climate

Deleted: .

Deleted: The five-year time slices were chosen to reduce the computational expense of the modelling (~24 hours per simulation), and the preceding decade was used to evaluate these time slices (Section 3.3).

Deleted: a

Deleted: rather than interpolating mass balance over time,

Deleted: Thus we arrived at the present-day simulation from the LIA simulation by forcing the LIA glacier with the 2015–2020 CE mass balance for 200 years. We use the output from the present-day simulation with the 2095–2100 CE mass balance to force the model to 2100 CE for a period of 80 years. We then use the result from this simulation as the starting point for the 2200 CE simulation forced by the 2195–2200 CE mass balance for 100 years, and the same approach for the 2300 CE using the 2295–2300 CE mass balance. Beyond 2100 CE less detailed climate projections are available; given the absence of regional climate projections, globally projected temperature changes were used to extend the end-of-century mass balances. These gave a further increase in temperature of 0.5°C by 2200 CE and 0.7°C by 2300 CE under RCP4.5, and 2.8°C by 2200 CE and 4.1°C by 2300 CE under RCP8.5 (Table 1; Collins et al., 2013). No precipitation changes were applied to the post-2100 CE climates due to the absence of projections for precipitation in the CORDEX RCMs and the high uncertainties associated with projections of global precipitation changes for this period. ¶

Deleted: We tested a range of lapse rates from $3.0^{\circ}\text{C km}^{-1}$ to km^{-1} based on the range of monthly values calculated from regression of NASA MODIS land surface temperature data for the Central Himalaya while maintaining the same ELA, which resulted in a difference in ice volume of $0.4 \times 10^9 \text{ m}^3$ and no change in glacier length at the present day.

Deleted: We examined the uncertainty in accumulation resulting from the application of a calculation to move snowfall from slopes susceptible to avalanching. ... [4]

Deleted: Khumbu Glacier

Deleted: the glacier model

Deleted: mass balance

Deleted: ,

Deleted: W

Deleted: ,

Deleted: and the resulting glacier

427 and ten-day precipitation cycles were observed linked to oscillations in the Tibetan High. A new AWS
428 was installed at the Pyramid Observatory at 5,035 m a.s.l. in September 2000 as part of a network in
429 the Dudh Koshi valley of six AWS between 2,680 to 5,700 m a.s.l., in addition to some short-lived
430 higher-elevation stations, maintained by the Ev-K2-CNR network. The Pyramid Observatory AWS
431 included a snow depth sensor between 2009 and 2010, but the data were discontinuous and inconsistent,
432 and the measurement period ended in December 2010. A second AWS was installed in the same location
433 by the GlacioClim network in 2013 (Wagon et al., 2013; Sherpa et al., 2017) provides a longer period
434 of continuous data collection. More recently, a network of 5 AWS including the highest elevations in
435 the Khumbu catchment were installed by the National Geographic project at Phortse (3,810 m a.s.l.),
436 Everest Base Camp (5,315 m a.s.l.), Camp 2 (6,464 m a.s.l.), the South Col (7,945 m a.s.l.) and the
437 Balcony (8,430 m a.s.l.) (Matthews et al., 2020). However, at time of writing, there are no continuous
438 records of high-elevation meteorological variables that span a longer period than 15 years, making the
439 calculation of climate normals impossible. In this study, we analysed data from these various sources
440 for evaluation of mesoscale trends in the upper Khumbu Valley and for use to downscale RCMs and
441 evaluate the results of our calculations. The location of the AWS is shown in Fig. 1C. Gaps in the air
442 temperature and precipitation data were filled using interpolated data from neighbouring stations where
443 required (as described in Appendix A).

444
445 The AWS data were used to make a reference simulation in COSIPY of the surface energy fluxes and
446 mass balance of the Khumbu Glacier catchment between 2013–2015 for model development and
447 sensitivity experiments (Fig. 4 and Fig. 5). We compiled 14 years of meteorological observations from
448 the two AWS provided by the GlacioClim network at the Pyramid Observatory (5,050 m a.s.l. and 5,035
449 m a.s.l.) and the West Changri Nup Glacier AWS (5,363 m a.s.l.) (Wagon et al., 2013; Sherpa et al.,
450 2017). All meteorological data were collected for the period December 2010 to November 2019, apart
451 from precipitation which was only recorded between December 2012 to November 2016. All
452 meteorological data (excluding precipitation) used for the reference simulation were taken from the
453 West Changri Nup AWS. Given the frequency of missing precipitation data from the AWS, the
454 undercatch of snow associated with tipping bucket rain gauges, and the scarcity of high-elevation
455 precipitation measurements, precipitation was not varied with elevation in the reference simulation.
456 Precipitation data for the reference simulation were collected from the GlacioClim Geonor precipitation
457 gauge at the Pyramid Observatory (5,035 m a.s.l.) because this precipitation gauge provides a longer
458 period of continuous observations than the other gauges and avoids errors due to low precipitation
459 amounts measured by tipping bucket gauges, which are known to systematically underestimate snowfall
460 particularly during high winds (Sherpa et al., 2017). Precipitation was measured at 15-minute intervals
461 using a Geonor T-200BM sensor mounted 1.8 m above the surface. Evaporation from the bucket was
462 blocked by a layer of oil, but some loss did occur, as evidenced by precipitation values below 0 mm.
463 Noise from wind and evaporation were corrected for by compensating any negative change over the
464 15-minute time step with the neighbouring positive value such that accumulated precipitation was
465 unchanged. Periods with prolonged evaporation were set to zero. Undercatch of snowfall by rainfall
466 gauges was corrected through precipitation phase partitioning using wind speed observations (Wagon
467 et al., 2009). Air temperature was interpolated to match the height of the precipitation gauge using
468 hourly lapse rates that averaged $-5.89\text{ }^{\circ}\text{C km}^{-1}$. COSIPY was run for both elevations using the non-
469 adjusted temperature data for 5,336 m a.s.l. and the adjusted temperature data for 5,035 m a.s.l. and it
470 made little impact on the model results. Simulated meteorological variables were evaluated at the
471 highest elevations using the National Geographic AWS stations at Camp 2 (6,464 m a.s.l.) and the South
472 Col (7,945 m a.s.l.) using data for May–November 2019 (Matthews et al., 2020).

473
474 Direct solar radiation across the model domain was corrected for the slope, azimuth, and shadowing
475 potential of each pixel (Wohlfahrt et al., 2016; Sauter et al., 2020). A footprint-weighted correction was
476 also applied to horizontal measurements of net radiation. The fraction of diffuse incoming shortwave
477 radiation was estimated by using the ratio of total shortwave (global) radiation and potential shortwave
478 radiation to define a clearness index (Wohlfahrt et al., 2016). This clearness index was used to calculate
479 diffuse radiation, which was calibrated with data from the Neustift eddy covariance station in the
480 Austrian Alps (Wohlfahrt et al., 2008). Pressure was distributed across the domain by first calculating
481 sea-level pressure (*cf.* Lente and Osz, 2020) and then interpolated with the barometric equation. The

482 relative humidity gradient was calculated as $-0.002\% \text{ m}^{-1}$ using data from the Ev-K2-CNR and the
483 GlacioClim AWS networks, and evaluated by comparison with measurements made by the National
484 Geographic network AWS ranging in elevation from 3,810–8,430 m a.s.l. (Matthews et al., 2020) to
485 capture trends at higher elevations. The distributed radiative fluxes were compared with the same high-
486 elevation stations for 2019 to assess the efficacy of this method across the domain. Wind speed was
487 assumed to be uniform across the domain.

488 2.3 Present-day RCM downscaling using meteorological observations

489 Six RCMs were assessed on their fidelity to present-day climate using hindcasting (Biemans et al.,
490 2013) with an emphasis on temperature seasonality and seasonal precipitation dynamics given the
491 importance of these variables for glacier mass balance. RCMs from the Coordinated Regional
492 Downscaling Experiment (CORDEX) South Asia domain were dynamically downscaled from CMIP5
493 GCMs by the Indian Institute of Tropical Meteorology to a 50 km spatial resolution (Lutz et al., 2016)
494 and collected for the grid box containing Khumbu Glacier (27.9065056°N, 86.4352951°E). Three of
495 the six CORDEX South Asia RCMs (NOAA, CCCma, IPSL) spanning a range of possible future
496 precipitation conditions (Table 1) were selected as discrete scenarios for the glacier surface energy and
497 mass balance calculations. The three remaining RCMs were discounted due to being intermediate to
498 those selected for our experiments (i.e. close to the future precipitation scenario represented by CCCma)
499 or particularly poor at reproducing seasonal temperature and precipitation cycles. For example, despite
500 the annual precipitation sums from the CSIRO RCM being closest to observed values and having the
501 potential to be the ‘driest’ scenario examined, analysis of precipitation seasonality indicated that
502 the monsoon signal was completely absent with this RCM instead showing a strong dominance of winter
503 precipitation.

504
505 The present-day RCM results were downscaled using quantile mapping, also known as “distribution
506 mapping”, using 14 years of observations collected between January 2006 and November 2019 from
507 three AWS as described in Section 2.2. Parametric quantile mapping (Piani et al., 2010) was used to
508 downscale the RCM to a daily time step at the resolution of the DEM, whereby a statistical relationship
509 between the raw climate model outputs and observations was formed by substituting the RCM results
510 with observations at a cumulative density function of the prescribed distribution (e.g., a Gaussian
511 distribution for temperature; Luo et al., 2018; a gamma distribution for precipitation; Piani et al., 2010).
512 This correction was applied to the raw RCM outputs to produce a third downscaled dataset which had
513 an improved fit to the observations (Fig. 2C and 2D). The quantile mapping approach was chosen
514 because this is effective for downscaling precipitation and reduces errors in the standard deviation,
515 the coefficient of variation, and the skewness of distributed values relative to other methods (Lafon et al.,
516 2013; Reiter et al., 2018). The AWS data were used to disaggregate the daily downscaled present-day
517 and end-of-century climate model outputs to an hourly resolution for energy balance modelling. All
518 meteorological variables, excluding precipitation, were downscaled using the MELODIST Python tool
519 (Förster et al., 2016). Seasonal means were applied for precipitation to reproduce the ‘nocturnal peak’
520 seen during the monsoon that MELODIST was unable to replicate (Figs. A1, A2 and A3). Further
521 information on the meteorological data analysis and RCM downscaling are provided in Appendix A.

522 2.4 Future RCM downscaling

523
524 Two future emission scenarios (RCP4.5 and RCP8.5) were available from CORDEX South Asia, which
525 represent intermediate and high emissions by 2100 CE relative to the present day. These two emissions
526 scenarios are frequently used in climate impact studies enabling the comparison of our results with
527 studies that use other climate/glacier model projections. The two future emissions scenarios were
528 analysed for each of the three CORDEX RCMs to account for the inherently high uncertainties in future
529 precipitation trends associated with climate models and the interplay of changing precipitation with
530 atmospheric warming. The same statistical downscaling approach and disaggregation used for the three
531 present-day RCMs described in Section 2.3 was applied to the raw CORDEX RCM daily outputs for
532 the three future RCM time slices under RCP4.5 and RCP8.5. The temperature change between the
533 present day and the future time slices was preserved and there was no evidence of any imposed
534 strengthening in the monsoon resulting from downscaling. An increase in the frequency of days per
535 year outside of the monsoon season with high precipitation amounts (defined here as over 15 mm of

Deleted: ¶

Deleted: 2

Deleted: ¶

Deleted: S

Deleted: ,

Deleted: were

Deleted: downloaded

Deleted: ,

Deleted: three automatic weather stations

Deleted: (AWS; Fig. 1c and Appendix A) collected between January 2006 and November 2019

Deleted: with gaps filled using interpolated data from neighbouring stations if required (Fig. 2).

Deleted: g

Deleted: with

Deleted: (

Deleted: Maraun et al., 2016)

Deleted: also

Deleted: resultant

Deleted: and AWS data analysis

Deleted: 3

Deleted: only

Deleted: (

Deleted: 2)

Deleted: this

562 daily precipitation) accounted in large part for the higher annual precipitation amounts relative to the
563 present day that were found in four out of the six RCMs. However, the total future annual precipitation
564 increase was on average 8.8% greater in the downscaled climates relative to the raw RCMs, suggesting
565 that this positive trend was inflated by downscaling. The downscaled climates reduced the frequency
566 of precipitation, although, as in present day observations, monsoon precipitation occurred frequently
567 and could be characterised as predominantly drizzle in the future.
568

569 2.5 Surface energy balance modelling

570 COSIPY is a leading open-source method for estimating glacier surface mass balance and has
571 previously been applied to glaciers in High Mountain Asia. COSIPY includes a calculation of
572 sublimation, which is an important ablation process for high-elevation glaciers because ablation can
573 still occur if the latent heat flux is negative through sublimation, even in instances where surface
574 temperature and/or air temperature are well below the melting point (Bonekamp et al., 2021; Brun et
575 al., 2023; Huintjes et al., 2015). COSIPY resolves all energy fluxes (F) at the ice surface that contribute
576 to surface melt (Q_{melt}):
577

$$578 F = SWin \cdot (1-\alpha) + LWin + LWout + Qsens + Qlat + Qg + Qliq \quad \text{Eq. (1)}$$

580 Where $SWin$ is incoming shortwave radiation, α is albedo, $LWin$ and $LWout$ are incoming and outgoing
581 longwave radiation, and $Qsens$, $Qlat$, and Qg are the sensible, latent, and ground heat fluxes (Oerlemans
582 et al., 2001) and $Qliq$ is the heat flux from liquid precipitation; the latter variable is often neglected
583 in ablation calculations (Cuffey and Paterson, 2010) but is of particular importance here as the Indian
584 Summer Monsoon brings a significant amount of liquid precipitation to the lower reaches of Khumbu
585 Glacier. The resulting F is equal to the energy available for surface melt (Q_{melt}) when surface
586 temperature (T_s) is at melting point (0°C). T_s is used to calculate $LWout$, $Qsens$, $Qlat$, Qg and to partition
587 solid and liquid precipitation. When T_s exceeds the melting point it is reset to 0°C (273.15 K) and the
588 residual F fluxes equal Q_{melt} . In this instance, subsurface melt is triggered when the energy fluxes, for
589 example, penetrating $SWin$ warm the ice layer so that T_s exceeds the melting point of ice (Sauter et al.,
590 2020).
591

592 The COSIPY model domain was taken from the 30-m DEM that was resampled to 200-m grid spacing
593 following a reference simulation for 2013–2015 and sensitivity analyses, which revealed minimal
594 impact on the results whilst greatly reducing computational expense (Fig. 4). The sensitivity of glacier
595 mass balance to individual meteorological variables (MAAT, radiative fluxes, relative humidity, lapse
596 rate, precipitation amount, precipitation phase, glacier surface roughness) was calculated in sensitivity
597 experiments using the reference simulation that perturbed these variables individually. Perturbations
598 were made within the range of the possible uncertainties for each variable that arise from a combination
599 of the choice of observations or climate models, the downscaling approach used, and the distribution of
600 meteorological variables. The values used for perturbations of MAAT and precipitation amount were
601 similar to those expected for possible future climate forcings.
602

603 The downscaled and disaggregated CORDEX RCM daily climate variables (temperature, precipitation,
604 the radiation components, wind speed, relative humidity and atmospheric pressure) were used to force
605 COSIPY for the periods 2015–2020 CE and 2095–2100 CE. While snowfall measurements can be used
606 as an input to COSIPY, there are no good-quality measurements of snowfall in the Everest region and
607 so precipitation was partitioned into rainfall and snowfall using the snow transfer scheme within
608 COSIPY (Sauter et al., 2020). COSIPY was forced using hourly meteorology with nine variables to
609 calculate the energy balance and mass balance components at an hourly time step from the sum of
610 accumulation by solid precipitation, deposition, and refreezing of melt water percolation, and ablation
611 by melt and sublimation. The exchange processes at the surface, including energy release and
612 consumption with phase changes, control temperature distribution and phase changes within the glacier
613 (comprised of horizontal ice and snow layers), and accounts for meltwater refreeze and percolation with
614 the meltwater produced from the surface melt calculations acting as an input. The impacts of
615 supraglacial debris on ablation and of snow avalanching on accumulation were handled in JSOSIA, as
616 described in the next section.

Deleted: 4

Deleted: COSIPY

Deleted: s

Deleted: COSIPY is a glacier surface energy and mass balance model that integrates a surface energy and mass balance model with a multi-layer snow and ice model (Weidemann et al., 2018; Sauter et al., 2020).

Deleted: was chosen as it is currently considered

Deleted: integrates a surface energy balance model with a multi-layer snow and ice model and thereby

Formatted: Font: Not Italic

Formatted: Font: Not Italic

Formatted: Normal, Don't add space between paragraphs of the same style

Deleted: that

Deleted: S

Deleted: , but

Deleted: given the paucity of observations and high uncertainties associated with AWS observations, climate reanalysis, and modelled snowfall products for this region

Deleted: . The coupling of the surface energy balance component with a multi-layer subsurface snow and ice model

Deleted: The mass balance was calculated at an hourly resolution, with accumulation resulting from the accumulation of solid precipitation on the ice surface, refreeze of meltwater, and deposition of water vapour, and ablation resulting from subsurface and surface melt and sublimation (Sauter et al., 2020).

Deleted: the glacier model

642

643 **2.6 Ice-dynamical glacier evolution modelling**

644 The second-order shallow ice approximation model (iSOSIA) is a 3-D higher-order ice-dynamical
645 glacier evolution model that solves for the flow of ice including longitudinal and transverse stress
646 gradients that are imposed on ice flow through high-relief topography (Egholm et al., 2011). This glacier
647 model simulates the evolution of debris-covered glaciers by incorporating the feedbacks between debris
648 transport, mass balance and ice flow (Rowan et al., 2015) and includes two processes that are important
649 for many Himalayan glaciers: (1) the redistribution of snow by avalanching that is estimated to account
650 for up to 75% of accumulation, and (2) the formation and evolution of a supraglacial debris layer that
651 insulates the ice surface to modify ablation (Rowan et al., 2015). While previous versions of this glacier
652 model used depth-integrated ice flow, this version simulates ice flow through Khumbu Glacier in 3-D
653 as the ice thickness is divided into 20 vertical layers to calculate englacial debris transport (Rowan et
654 al., 2015). The glacier model has a variable time step that can adjust up to a maximum of 0.1 years to
655 allow greater computational efficiency.

656

657 The distributed surface mass balances calculated using COSIPY using the downscaled RCMs for the
658 periods 2015–2020 CE and 2095–2100 CE were used as inputs to the glacier model with no change in
659 forcing applied between time steps. Surface processes within the glacier model modified the distribution
660 of accumulation and ablation but this was not updated into the surface topography used in COSIPY.
661 Simulated accumulation was the result of the total snowfall in each cell and avalanching of snow
662 imposed for the accumulated snowpack from hillslopes by removing snow and ice from hillslopes
663 greater than 28° and redistributing this mass across less steep surfaces using a non-linear hillslope flux
664 model (Roering et al., 1999). The avalanching routine was found to be sufficient to prevent snow and
665 ice accumulation on slopes that are observed to be free of glacier ice such as the southwest face of
666 Sagarmatha (Mt. Everest) while allowing accumulation on steep sections of the glacier (Rowan et al.,
667 2015) resulting in accumulation rates at the glacier surface in line with the limited available
668 observations for Himalayan glaciers of 2 m water equivalent (w.e.) per year (Benn and Lehmkuhl,
669 2000).

670

671 Rock avalanching is responsible for much of the debris accumulation on the glacier surface but there is
672 little information about the magnitude and frequency of these events, so headwall erosion was assumed
673 to be uniform at 1 mm a⁻¹ (Rowan et al., 2021). Debris produced by headwall erosion was delivered to
674 the glacier surface using a similar non-linear hillslope flux model to snow avalanching. The reduction
675 in ablation beneath supraglacial debris from clean-ice values was represented as a reciprocal function
676 that scaled clean-ice ablation (b_{clean}) to give sub-debris melt (b_{debris}) as a function of debris thickness
677 (h):

678

679
$$b_{debris} = b_{clean} \times \frac{h_0}{h+h_0} \quad \text{Eq. (2)}$$

680

681 where h_0 is a constant representing the characteristic debris thickness at which the reduction in ablation
682 due to insulation by supraglacial debris is 50% of the value for an equivalent clean-ice surface
683 (Anderson and Anderson, 2016; Rowan et al., 2021). The observed heterogeneity of surface ablation
684 required a parameterisation of sub-debris melt representing the effects of differential ablation, which
685 was represented in Equation (2) using a value for h_0 of 0.8 m (Bartlett et al., 2021; Rowan et al., 2021;
686 Strickland et al., 2023). We note that Equation (2) represents an empirical calculation of the impact of
687 supraglacial debris on glacier surface melt that is calibrated to observations of sub-debris melt rates for
688 glaciers in the Central Himalaya (Rowan et al., 2021) and as such, changes in surface energy balance
689 processes including vapour fluxes within the debris-covered section of the glacier are not included.

690

691 **3. Results**

692 **3.1 COSIPY parameter perturbations**

693 The spatially averaged mass balance was most sensitive to changes in MAAT (perturbed by ±1.5°C,
694 2.0°C and 3.0°C), $LWin$ and $SWin$ (±10% and 20%). Perturbations of relative humidity (±10% and
695 ±20%) had the least impact on mass balance. The use of a seasonal lapse rate of 5.38°C km⁻¹ yielded a

Deleted: 5

Deleted: G

Formatted: Font: Bold

Deleted: —

Deleted: the evolution

Deleted: of

Deleted: ¶

The sensitivity of glacier mass balance to individual meteorological variables (MAAT, radiative fluxes, relative humidity, lapse rate, precipitation amount, precipitation phase, glacier surface roughness) was calculated in experiments that perturbed these variables individually. Perturbations were made within the range of the possible uncertainties for each variable that arise from a combination of the choice of observations or climate models, the downscaling approach used, and the distribution of meteorological variables. The values used for perturbations of MAAT and precipitation amount were similar to those expected for possible future climate forcings. ¶

714 spatially averaged mass balance that was 5.6% less than the reference calculation value, while a diurnal
 715 lapse rate gave a mass balance that was only 0.45% lower because the reference lapse rate was close to
 716 the mean of the day/night lapse rates, whereas ~~the~~ environmental lapse rate ($6.50^{\circ}\text{C km}^{-1}$) gave a mass
 717 balance that was 1.24% higher than the reference value. The relatively small difference in mass balance
 718 due to the choice of lapse rate is due to the extremely high elevation of Khumbu Glacier, which means
 719 that MAAT is below 0°C in the accumulation area for much of the year and a higher lapse rate does not
 720 affect rain/snow partitioning. The largest difference in mass balance due to the choice of lapse rate
 721 ~~occurred just below the ELA and resulted in a difference of $\pm 24\%$ in spatially averaged mass balance~~
 722 ~~for this section of the glacier.~~ The National Geographic AWS on Mt. Everest provided an opportunity
 723 to examine lapse rates at the highest elevations. For the period April–November 2019, the observed
 724 lapse rate was $4.68^{\circ}\text{C km}^{-1}$ between Phortse (3,810 m a.s.l.) and Everest Base Camp (5,315 m a.s.l.),
 725 and $5.36^{\circ}\text{C km}^{-1}$ between Camp II and South Col, similar to the value used in this study. The lapse rate
 726 above 8,000 m a.s.l. was about $1.2^{\circ}\text{C km}^{-1}$ greater than that below 5,600 m a.s.l. between the two highest
 727 AWS ~~at the~~ South Col (7,945 m a.s.l.) ~~and the~~ Balcony (8,430 m a.s.l.) indicating that in the highest-
 728 elevation sections of the catchment, lapse rates may be best represented by values considered suitable
 729 for the free atmosphere.

731 Coupled parameter testing ~~was carried out to~~ perturb precipitation and MAAT simultaneously. The most
 732 significant change in spatially averaged mass balance followed a 3°C increase in MAAT and 20%
 733 decrease in precipitation amount. The change in ablation following an increase in temperature of 1.5°C
 734 was compensated by accumulation resulting from 20% higher precipitation. The impact on mass
 735 balance of two precipitation phase (rain/snow) partitioning schemes was investigated and compared
 736 with the default snow transfer function in COSIPY; (1) using threshold temperatures of 0.5°C , 2.0°C ,
 737 and 3.5°C , and (2) using a calculation that smoothly scaled rain/snow partitioning from 100% solid
 738 precipitation at -1°C to 0% solid precipitation at 4°C . The height of the 0°C isotherm during months
 739 that experienced significant ablation (May–September) fluctuated around 5,125–6,250 m a.s.l., which
 740 correlated with the elevations that experienced the greatest mass balance change with lapse rate. While
 741 the lapse rate used to distribute MAAT did not have a significant impact on glacier-wide mass balance,
 742 the elevation of the 0°C isotherm from the pre-monsoon until the end of the monsoon was sensitive to
 743 the air temperature distribution.

745 The glacier ice surface roughness (z_0) value was 1.7 mm (Table 2), which is a reasonable estimate for
 746 clean-ice glaciers (Mölg et al., 2012). The z_0 values reported in the literature vary widely, even for clean-
 747 ice glaciers, and do not consider debris-covered glacier surfaces, and so two substantially different z_0
 748 values were tested as end-members of the likely range in z_0 values for Khumbu Glacier. Values for z_0 of
 749 0.1 mm from Midtre Lovénbreen in Svalbard (Irvine-Fynn et al., 2014) and August-One Glacier in
 750 China (Guo et al., 2018), and a value of 6.9 mm for the clean-ice section of Haut Glacier D’Arolla
 751 (Brock et al., 2006) were all tested in the reference simulation. Adjusting z_0 had minimal impact on
 752 mass balance, although a higher (lower) z_0 did result in slightly increased (decreased) mass balance.

755 3.2 Evaluation of the COSIPY surface energy balance model results

756 The reference simulation represented the period 2013–2015 CE and was forced with AWS data using
 757 the model parameters in Table 2. Turbulent fluxes and energy balance components across Khumbu
 758 Glacier were explored across the 2013–2015 reference period to assess the performance of COSIPY
 759 and understand their relative spatial importance (Fig. 5). The glacier-wide clean-ice mass balance for
 760 the three-year reference period was -3.4 m w.e., which equates to -1.13 m w.e. a^{-1} . Maximum ablation
 761 was up to 16.2 m w.e. over three years (Fig. 4). High precipitation events were observed to offset some
 762 ablation if they occurred outside the core monsoon season (e.g., in October 2013 and May 2014) but
 763 did not influence monsoon season ablation when high air temperatures and strong incoming radiative
 764 fluxes rapidly remove snow cover and drive melting. Higher minimum temperatures in winter 2013–
 765 2014 CE relative to the other winters did not significantly influence accumulation rates, which remained
 766 similar to those in 2014–2015 CE. Low precipitation amounts during the 2015 monsoon (286 mm in
 767 2015, compared to 330.8 mm in 2013, and 333.9 mm in 2014) resulted in lower accumulation in the
 768 upper reaches of the glacier. The precipitation gradient was calibrated to $1 \times 10^{-5} \% \text{ m}^{-1}$ to match

Deleted: the

Deleted: was

Deleted: of $\pm 24\%$

Deleted: installation of the

Deleted: automatic weather stations

Deleted: in 2019

Deleted: .

Deleted: (

Deleted: The glacier ice surface roughness (z_0) value was 1.7 mm (Table 2), which is a reasonable estimate for clean-ice glaciers (Mölg et al., 2012). The z_0 values reported in the existing literature vary widely even for clean-ice glaciers and do not consider debris-covered glacier surfaces, and so two substantially different z_0 values were tested as endmembers of the likely range in z_0 values; 0.1 mm from Midtre Lovénbreen in Svalbard (Irvine-Fynn et al., 2014) and August-One Glacier in China (Guo et al., 2018), and 6.9 mm for the clean-ice section of Haut Glacier D’Arolla (Brock et al., 2006). Adjusting z_0 had minimal impact on mass balance, although a higher (lower) z_0 did result in slightly increased (decreased) mass balance. ¶

Deleted: involved

Deleted: ing

Deleted: COSIPY

Deleted: and mass

Moved (insertion) [5]

Deleted: by

Deleted: (Appendix A)

Deleted: ¶

Deleted: a three-year

Moved (insertion) [6]

798 observed accumulation rates. However, this gradient largely arises from avalanching (Benn and
799 Lehmkuhl, 2000) which is challenging to represent in COSIPY and was instead handled in the glacier
800 model (Section 2.6).

801 The energy available for ablation peaked in the pre-monsoon and monsoon, bringing higher rates of
802 sublimation and subsurface melt in April–June (Fig. 5). Simulated sublimation occurred at all
803 elevations, with the highest cumulative loss near the South Col (EB7910) where sublimation dominated
804 mass balance and only slightly slowed from December until May. Sublimation rates were increasingly
805 tied to seasonality with distance down-glacier, with rates on the lower section of the tongue (EB4980)
806 increasing from April until the start of the monsoon in July. Calculated subsurface melt was negligible
807 at or above the ELA (5,950 m a.s.l.) whereas at lower elevations sub-surface melt dominated mass
808 balance with a stronger seasonal cycle related to surface temperature. The interannual variability in
809 subsurface melt was linked to surface temperature, although low simulated subsurface melt rates in the
810 first year of the reference simulation were largely due to persistence of the initial snow cover that
811 shielded the subsurface from relatively warm air temperatures until the subsurface adapted to local
812 conditions. Refreezing occurred across the entire glacier, with a staggered onset due to increased
813 elevation, and the absolute values were low (Fig. 5). The higher latent heat flux during the monsoon
814 resulted in higher deposition of snow to the glacier at the lower elevations, with negligible rates at
815 higher elevation. Similar absolute values and patterns are seen for condensation.

816 Calculated incoming shortwave radiation matched well with AWS observations, indicating that the
817 radiation model in COSIPY performed well across the extreme relief of the Khumbu Glacier catchment.
818 Net shortwave radiation contributed the largest energy input to the glacier surface at lower elevations,
819 correlating most strongly with the energy available for melt, with a mean correlation coefficient of 0.79.
820 There was high temporal variability related to variable cloud cover exhibited in the hourly incoming
821 shortwave radiation forcing and fluctuating albedo during the warmer months with the melting of the
822 snowpack. The high incoming shortwave radiation the upper reaches of the glacier indicate that low net
823 shortwave radiation is not due to topographic shading. Net shortwave radiation was correlated with
824 albedo ($r = 0.86$), and the persistence of snow throughout much of the year reduced the energy available
825 for melt. Net longwave radiation also contributed to the energy available for melt as the pattern of both
826 fluxes corresponded. Between 5,900–7,900 m a.s.l., net longwave radiation sometimes exceeded zero
827 during the monsoon, most likely due to heavy cloud cover and increased temperatures relative to the
828 glacier surface. The latent heat flux was almost zero at the lower elevation sites as the arrival of the
829 monsoon resulted in higher relative humidity, and this pattern was similar, but dampened, at higher
830 elevation. At the South Col (EB7910) the energy available for melt correlated exactly ($r = 1$) with the
831 sensible heat flux (Fig. 5).

832 Grid spacings for the model domain of 30 m, 50 m, 200 m and 1 km were tested to ensure that that the
833 COSIPY calculations captured orographic effects without unnecessary computational expense (Fig. 4).
834 The simulated maximum accumulation rate did not change significantly with grid spacing, giving
835 accumulation rates of 2.1–3.9 m w.e. at 6,500–7,000 m a.s.l. in the reference simulation. The 1 km grid
836 spacing contained only 27 glacier points, and gave a similar spatial mean mass balance to the finer-
837 resolution calculations, but there were large gaps in mass balance calculated across the glacier that
838 affected the height of the ELA and significantly reduced the calculated maximum accumulation value.
839 The 30-m and 50-m grid spacings captured greater spatial variability in mass balance relative to the 200
840 m resolution calculation, particularly at elevations between 5200–5400 m a.s.l. (Fig. 4). However, as
841 the ELA, and the calculated maximum and minimum mass balances were not significantly different
842 between these finer-resolution calculations, the 200 m grid spacing was used throughout to benefit from
843 the much reduced computational expense.

844 3.3 Evaluation of the RCM downscaling

845 The downscaled climate variables from the three RCMs for the present-day time slices (2015–2020 CE)
846 were evaluated against 14 years of observations from three AWS to assess the representation of means,
847 seasonality, diurnal cycles, day-to-day variability, and interannual variability (Fig. 2C and 2D). All three
848 downscaled RCMs showed good agreement between mean annual air temperature ($-2.15 \pm 0.05^\circ\text{C}$) and

Deleted: 5

Moved up [5]: The reference simulation represented the period 2013–2015 CE and was forced by AWS data (Appendix A) using the model parameters in Table 2.

Deleted: ¶

A reference simulation was made using COSIPY for comparison with observed glacier mass balance and tested across a range of grid spacings (30 m to 1 km).

Deleted: ¶

COSIPY was used to calculate clean-ice surface mass balance from the downscaled RCMs, and the insulating effects of supraglacial debris were calculated in the glacier model.

Moved up [6]: The glacier-wide clean-ice mass balance for the three-year reference period was -3.4 m w.e., which equates to -1.13 m w.e. a^{-1} . Maximum ablation was up to 16.2 m w.e. over three years (Fig. 4). High precipitation events were observed to offset some ablation if they occurred outside the core monsoon season (e.g., in October 2013 and May 2014) but did not influence monsoon season ablation when high air temperatures and strong incoming radiative fluxes rapidly remove snow cover and drive melting. Higher minimum temperatures in winter 2013–2014 CE relative to the other winters did not significantly influence accumulation rates, which remained similar to those in 2014–2015 CE. Low precipitation amounts during the 2015 monsoon (286 mm in 2015, compared to 330.8 mm in 2013, and 333.9 mm in 2014) resulted in lower accumulation in the upper reaches of the glacier. The precipitation gradient was calibrated to $1 \times 10^{-5} \text{ m}^{-1}$ to match observed accumulation rates. However, this gradient largely arises from avalanching (Benn and Lehmkuhl, 2000) which is challenging to represent in COSIPY and was instead handled in the glacier model (Section 2.5).

Deleted: 5) ¶

The energy available for ablation peaked in the pre-monsoon and monsoon, bringing higher rates of sublimation and subsurface melt in April–June (Fig. 5). Simulated sublimation occurred at all elevations, with the highest cumulative loss near the South Col (EB7910) where sublimation dominated mass balance and only slightly slowed from December until May. Sublimation rates were increasingly tied to seasonality with distance down-glacier, with rates on the lower section of the tongue (EB4980) increasing from April until the start of the monsoon in July. Calculated subsurface melt was negligible at or above the ELA (5,950 m a.s.l.) whereas at lower elevations sub-surface melt dominated mass balance with a stronger seasonal cycle related to surface temperature. The interannual variability in subsurface melt was linked to surface temperature, although low simulated subsurface melt rates in the first year of the reference simulation were largely due to persistence of the initial snow cover that shielded the subsurface from relatively warm air temperatures until the subsurface adapted to local conditions. Refreezing occurred across the entire glacier, with a staggered onset due to increased elevation, and the absolute values were low (Fig. 5). The higher latent heat flux during the monsoon resulted in higher deposition of snow to the glacier at the lower elevations, with negligible rates at higher elevation. Similar absolute values and patterns are seen for condensation.

Deleted: observations from Ev-K2-CNR, GlacioClim, and high-elevation

Deleted: networks

Deleted: (Matthews et al., 2020)

Deleted: (Fig. 6)

Deleted: 6

Deleted: for the climate-glacier model

Deleted: (Fig. 4)

Deleted: ¶

940 observed air temperature from the Pyramid AWS (Figs. A1 and A2). The representation of the monsoon
 941 was greatly improved by the RCM downscaling; temperature seasonality was well resolved following
 942 quantile mapping and the monthly mean and minimum air temperatures were similar to observations
 943 across the present-day time slice (Fig. A1). The monsoon stabilised air temperatures and reduced the
 944 range between minimum and maximum temperatures in the downscaled RCMs, which was in better
 945 agreement with AWS observations, but was not present in the raw RCMs prior to downscaling. We note
 946 that the downscaled maximum air temperature was at times higher than observations amongst all RCMs
 947 during the post-monsoon and winter (Fig. A1) but the distribution of downscaled air temperatures was
 948 similar to observed values (Fig. A2). Gamma-distribution quantile mapping substantially improved the
 949 absolute precipitation values relative to the AWS observations compared to those in the raw RCMs; the
 950 overestimation of winter precipitation and relative underestimation of monsoon precipitation amounts
 951 in the raw RCMs was reduced and downscaled results show a clearer monsoon signal (Fig. A3). When
 952 compared with AWS observations, RCM downscaling slightly overcorrected the seasonal precipitation
 953 pattern with a slight underestimation of winter precipitation for the most extreme winter events. Across
 954 the three present-day RCM simulations, the surface mass balance calculated using the NOAA RCM
 955 was more positive than that for the ISPL and CCCma RCMs and most similar to the mass balance
 956 calculated from meteorological observations, and remained the most positive mass balance in the end-
 957 of-century time slices (Fig. 6).

959 3.4 Evaluation of the iSOSIA glacier evolution model results

960 COSIPY was used to calculate clean-ice surface mass balance from the downscaled RCMs, and the
 961 insulating effects of supraglacial debris were calculated in iSOSIA. The simulated glacier geometry and
 962 dynamics were compared with remotely sensed observations of ice thickness, supraglacial debris
 963 distribution, velocity, and surface elevation change for the present-day glacier (Fig. 3) and varied
 964 depending on the RCM used as forcing (Fig. 7). The experiment using the NOAA RCM was identified
 965 as the starting point for all future simulations because this was most representative of the observed
 966 glacier at 2015 CE. The distributed surface mass balances calculated using COSIPY were most similar
 967 to observed values after the calculated surface mass balances were integrated with the glacier model to
 968 include accumulation by snow avalanching and the reduction in surface melting beneath supraglacial
 969 debris; the active glacier extent was underestimated if supraglacial debris is not simulated (Fig. 8). The
 970 supraglacial debris-mass balance feedback in the glacier model reproduced the observed reversed mass
 971 balance gradient and peak in ablation below the Khumbu Icefall (Fig. 1D).

972
 973 The simulated glacier area was 7.8 km² and similar to that obtained from structural mapping in 1979
 974 CE (Nakawo, 1986). Radio-echo sounding in 1999 CE obtained ice thickness estimates close to the
 975 active terminus of ~160 m (Gades et al., 2000) and simulated ice thickness at the terminus was 130 m
 976 (Fig. 3A). The simulated thickness at the active glacier terminus thickness was approximately 175 m in
 977 1999 CE, which agreed well with observations from DEMs of difference that show thinning here of up
 978 to 55 m between 1984–2018 CE (Fig. 3D and 3E) (King et al., 2020). Simulated surface elevation
 979 change in the ablation area was -30 m over 20 years to the present day and similar to values derived
 980 from satellite observations for 1984–2018 CE (King et al., 2020). Simulated present-day glacier
 981 velocities (Fig. 9) show a similar pattern and magnitude to glacier surface velocities observed using
 982 remote sensing observations, which reach a maximum of 220 m a⁻¹ in the Khumbu Icefall (Altena and
 983 Käab, 2020) and up to 20 m a⁻¹ in the ablation area (Quincey et al., 2009; Dehecq et al. 2019). The
 984 simulated present-day velocities in this study were a better fit to remote sensing observations than those
 985 from previous simulations that used an elevation-dependent mass balance forcing (Rowan et al., 2015,
 986 2021) where the maximum simulated velocities were 118 m a⁻¹.

988 3.5 Climate change and glacier evolution from the present day until 2100 CE

989 Khumbu Glacier is responding to historical climate change and will continue to shrink even if warming
 990 ceases today. Indeed, if we allow the spin-up experiment to reach equilibrium with the present-day
 991 NOAA RCM mass balance, the glacier terminus will recede by 2.1 km and the maximum ice thickness
 992 will decrease from 246 m to 206 m by 2100 CE without any additional warming. In this scenario, a
 993 supraglacial debris layer up to 1.3 m thick extends 1 km up-glacier from the terminus and partially
 994 dampens the committed volume loss, by sustaining 13% more ice volume than would be the possible

Deleted:

Deleted: (Appendix A)

Deleted: s

Deleted: ,

Deleted: that

Deleted:

Deleted: -

Deleted: simulations

Deleted: (Fig. 7)

Deleted: , and debris cover extent

Deleted: 8

Deleted: 5

Deleted: 9

Deleted: ¶

Deleted: (Fig. 10a)

Deleted: simulation

Deleted: s

Deleted: s

1013 for a clean-ice glacier surface with the same mass balance (Fig. 10A). The committed glacier volume
1014 loss due to historical warming in the absence of any further climate forcing is 10–23% of the present-
1015 day glacier mass (Fig. 10C) with the associated uncertainty represented by this range of values arising
1016 from the parameterisation of the impact of supraglacial debris evolution on surface melting.

1017
1018 Now considering the effects of additional warming under the RCP scenarios for the NOAA experiment,
1019 we find that greater warming occurs in winter than in summer under both RCPs and results in an
1020 increase in annual precipitation amount of about 15% made up of a greater increase in winter
1021 precipitation than summer precipitation (Fig. 2E). The climate forcing from the downscaled NOAA
1022 RCM under RCP4.5 is 1.4°C warmer than the present day (−0.75°C in 2095–2100 CE compared with
1023 −2.15°C in 2015–2020 CE) and annual precipitation increases by 14.8% from 581.4 mm at present day
1024 to 664.8 mm a^{−1} by 2100 CE with summer (June–September) precipitation increasing by 5.4% and
1025 winter (December–February) precipitation increasing by 14.1% (Fig. 2E). Under RCP8.5, the
1026 downscaled climate forcing is projected to be 3.8°C warmer than present day (1.65°C in 2095–2100
1027 CE) with an increase in annual precipitation of 14.9% by 2100 CE, with summer precipitation
1028 increasing by 9.8% and winter precipitation increasing by 19.4% (Fig. 2E).

1030 In the NOAA RCM RCP4.5 experiment, the spatially averaged cumulative glacier mass balance is −
1031 0.14 m w.e. a^{−1} in 2100 CE, which is slightly more positive than the present-day value of −0.21 m w.e.
1032 a^{−1} (Fig. 6) and glacier volume decreases by 36% between the present day and 2100 CE (Fig. 10C).
1033 While significant, this end-of-century glacier loss is partially offset by the concurrent increase in
1034 precipitation. In comparison, an equivalent simulation forced only by warming and without any change
1035 in precipitation results in a more linear trajectory of glacier change and 70% loss of glacier volume by
1036 2100 CE (cyan line in Fig. 10C) demonstrating that 34% of potential glacier loss from warming could
1037 be compensated by the increase in precipitation that occurs as a result of warming.

1039 3.6 Comparison of projections for different RCM forcings

1040 The CCCma and IPSL RCMs projected greater warming from the present day by 2100 CE than the
1041 NOAA RCM under RCP4.5 with a value of 1.6°C (+0.2°C compared with the NOAA RCM) in the IPSL
1042 RCM experiment and 2.2°C (+0.8°C) in the CCCma RCM experiment. These two RCMs also projected
1043 slightly greater warming by 2100 CE under RCP8.5, with a value of 3.9°C (+0.1°C compared with the
1044 NOAA RCM) for the IPSL RCM experiment and 4.1°C (+0.3°C) for the CCCma RCM experiment.

1046 The projected increase in precipitation amount across the three RCMs is similar between RCPs with
1047 annual totals above 600 mm by 2100 CE. The CCCma RCM gives the greatest increase in annual
1048 precipitation amount of 100 mm by 2100 CE (Fig. 2E). There is no evidence of change in the intensity
1049 of the Indian Summer Monsoon, as the seasonal split in precipitation remains similar to the present day,
1050 but the frequency of days with high precipitation (over 15 mm per day) increases by 2100 CE, giving
1051 twice as many days in the NOAA RCM experiment and up to seven times as many days in the IPSL
1052 RCM experiment.

1054 Under RCP8.5, all experiments showed similar results for mass balance by 2100 CE with only a 10%
1055 difference in glacier volume between the three RCMs (Fig. 10C). The CCCma RCM experiment has
1056 only a 1% difference in volume loss between RCP4.5 and RCP8.5 by 2100 CE despite a 1.9°C
1057 difference in MAAT—this is a surprising result given the significant temperature difference, which can
1058 be attributed to the greater number of high-magnitude precipitation events that occur under RCP8.5 in
1059 combination with the small difference in winter temperatures between the two RCPs. Indeed, in the
1060 CCCma RCM experiment under RCP4.5, the maximum winter temperature is 1.7°C higher than for the
1061 other RCMs, resulting in ablation and rainfall (rather than snowfall) during the winter.

1063 4. Discussion

1064 4.1 Uncertainties associated with the glacier modelling

1065 Sources of uncertainty in our results arose from each step of our glacier modelling workflow, and we
1066 considered how the experiments could be designed to reduce these uncertainties. Here we discuss the
1067 potential sources of uncertainty associated with the choice of RCMs, the downscaling of the RCMs, the

Deleted: 9b

Deleted: (Sanjay et al., 2017)

Deleted: . G

Deleted: light blue

Deleted: d

Formatted: Font: Bold

Deleted: d

Deleted: ¶

Deleted: 3.6 Climate change and glacier evolution from 2100 CE until 2300 CE ¶

Projections of climate change beyond 2100 CE are more uncertain than those for this century and the uncertainties associated with the model experimental design become larger, but these results do indicate a future trajectory for Khumbu Glacier. As there are no regional temperature projections beyond 2100 CE we used global values to continue the simulations into the next century (Table 1). However, there are no global projections of precipitation beyond 2100 CE and to avoid introducing potentially significant uncertainties to our results by estimating these values, no changes in precipitation were applied beyond 2100 CE. ¶

¶ In all the RCP4.5 experiments, there is little change in glacier volume between 2200 CE and 2300 CE compared with 2100 CE regardless of the RCM forcing used (Table 1 and Fig. 10b). In the NOAA RCP4.5 experiment, the Khumbu Icefall is maintained until 2300 CE and ice continues to flow from the Western Cwm to below 6,000 m so that the glacier remains in contact with the dynamically detached tongue. Therefore, keeping warming within the limit of RCP4.5 could restrict future volume loss to only 26% beyond that already committed to by historical climate change, and Khumbu Glacier would reach a new dynamic equilibrium that maintains a sufficient ice thickness to survive for at least two centuries. However, in all the RCP8.5 experiments, substantial glacier loss occurs after 2100 CE and Khumbu Glacier completely decays before 2300 CE. ¶

¶ Physical detachment of the debris-covered tongue from the active glacier, whereby this area contained no active glacier ice, occurs around 2140 CE in the NOAA experiment (Fig. 9) and around 2070 CE in the CCCma and IPSL experiments. We defined the glacier to be stagnant when the maximum rate of ice flow is less than 10 m a^{−1}; a conservative estimate of the uncertainty associated with observations of glacier velocities (Dehecq et al., 2019). Accordingly, we consider Khumbu Glacier to no longer be a viable glacier system at the point where there is no ice flow above this value in the entire glacier since there is minimal throughput of ice mass. In the NOAA RCP8.5 experiment, the glacier area is 1.2 km² and the mean velocity reduces to 10 m a^{−1} by 2260 CE, such that the glacier is no longer viable. Glacier breakdown occurs earlier for the CCCma and IPSL RCM experiments (Fig. 10b) by 2170–2180 CE because loss of ice volume due to warming is not compensated to the same magnitude by the increase in precipitation. ¶ [6]

Deleted: climate-

Deleted: approach

Deleted: climate-

Deleted: ,

Deleted: In this section

1176 use of time slices rather than continuous mass balance calculations, the representation of future
1177 precipitation in the RCMs, and the representation of avalanching in the glacier model.
1178

1179 A single RCM was not considered sufficient to represent both present-day climate and potential future
1180 climatic extremes, but the climate-mass balance forcing ensemble was limited in size due to the small
1181 number of RCMs available. The use of three RCMs allowed the implications of uncertainties in
1182 understanding of local climate for glacier evolution to be evaluated. A multi-model mean approach
1183 using all the CORDEX South Asia RCMs (as widely used elsewhere) was not considered sufficient to
1184 represent present-day and future climate conditions in the Khumbu Valley because this approach gives
1185 equal weighting to models irrespective of their performance (Pierce et al., 2009) and does not enable
1186 intercomparison of results for future climate conditions.
1187

1188 Five-year downscaled RCM time slices were chosen to reduce computational expense associated with
1189 COSIPY and the integration with iSOSIA. To ensure that the five-year periods selected were
1190 representative, the preceding decade was used for comparison with the time-slice results (results not
1191 shown). The use of quantile mapping with 14 years of AWS data as the downscaling method limited the
1192 influence of any natural variability by ensuring that the period did not reflect an extreme phase of natural
1193 climate oscillation. This comparison was particularly important for the future time slices, where large
1194 uncertainties arise between RCMs, and observational data cannot be used for evaluation of the
1195 downscaled climate or the resulting mass balance. We note that this experimental design could be
1196 improved by interpolating the mass balance over time and coupling the COSIPY and iSOSIA models
1197 such that mass balance was calculated dynamically for the evolving ice surface, but this was beyond
1198 the scope of our experiments. However, the experiments were repeated using additional mid-Century
1199 (2045–2050 CE) mass balance forcings to investigate if this produced a different end-of-Century result.
1200 These experiments produced near-identical results in 2100 CE to the experiments with no mid-Century
1201 forcing, in part because the response time of the simulated glaciers was longer than the 40-year period
1202 between the present-day and future time slices. Thus, a mid-century surface mass balance forcing was
1203 not considered necessary in our experiments and instead we used a step forcing for mass balance rather
1204 than interpolation between mass balance calculations in the glacier model.
1205

1206 The differences in simulated glacier change and response time between RCM forcings were at times
1207 greater than those resulting from the RCP due to differences in projections of precipitation. Whilst the
1208 three selected RCMs performed well in representing annual precipitation cycles from the six available
1209 CORDEX RCMs, we note that this representation was still fairly poor, although substantially improved
1210 by quantile mapping (Fig. 2D). The poor representation of monsoon dynamics in the present-day RCMs
1211 highlights an additional uncertainty associated with future precipitation scenarios and that these results
1212 should be treated as a set of possible scenarios.
1213

1214 The CORDEX CMIP5 and CMIP6 projects only produced dynamically downscaled RCMs for two
1215 future emissions scenarios (RCP4.5 and RCP8.5) and as such the implications of other RCPs for glacier
1216 evolution could not be assessed. The downscaled future climates were compared with those from other
1217 studies using CORDEX results, and showed similar annual and seasonal regional temperature trends
1218 strongly linked to the choice of RCP, and similar positive precipitation trends with poor agreement
1219 between RCMs (Kaini et al., 2019; Sanjay et al., 2017). The relationship between precipitation and
1220 warming in the two future emissions scenarios was less clear than that for air temperatures because the
1221 monsoon-influenced Himalaya has particularly poor RCM consensus and high levels of uncertainty in
1222 future precipitation trends with warming relative to other regions in High Mountain Asia (Sanjay et al.,
1223 2017).
1224

1225 A potentially large uncertainty in the glacier model arose from the parameterisation of avalanching, as
1226 this mass balance variable is poorly constrained, with no direct observations of the avalanche
1227 contribution to the mass balance of Khumbu Glacier and high regional variability (Kneib et al., 2025).
1228 Avalanching was included in iSOSIA by slope-dependent diffusion and resulted in increased
1229 accumulation along the glacier surface in the Western Cwm and improved the agreement between
1230 simulated and observed accumulation rates and distribution (Fig. 1D). Future work to resolve the impact

Deleted: the use of GCM forcing beyond 2100 CE,

Deleted: , as

Deleted: the glacier model

Deleted: Appendix A

Deleted: ¶

¶
The time slice approach resulted in a stepped response in terms of ice volume change over time where the forcing was changed (Fig. 10d). The glacier continued to evolve through each century rather than equilibrate with the mass balance forcing, but

Deleted: w

Deleted: stepped approach

Deleted: h

Deleted: ; however

Deleted: T

Deleted: c

Deleted: to simulate glacier evolution until 2100 CE

Deleted: c

Deleted: c

Deleted: The reacceleration in glacier mass loss after 2100 CE was in part due to the stepped forcing approach and the uncertainties associated with GCM projections, which increase with time after 2100 CE particularly under RCP8.5. For example, forecasts of global warming for 2281–2300 CE relative to 1986–2005 CE under RCP8.5 range from 3.0°C to 12.6°C (Collins et al., 2013).

Deleted: that resulted from the

Deleted: s

Deleted: s

Deleted: relatively

Deleted: The transition in the glacier model between the downscaled RCM and the GCM forcing could be improved by homogenising the climate model results across 2090–2100 CE, however, as noted above, the computational expense of forcing COSIPY with downscaled RCM outputs to create inputs to the glacier model required the use of a time-slice approach that was limited to five-year periods, and integration of the RCM results with GCM results was beyond the scope of this study. In the absence of RCMs that can project changes in precipitation after 2100 CE, precipitation was maintained at the same level for the glacier surface energy and mass balance model simulations beyond 2100 CE. The end-of-century precipitation amount is therefore unlikely to be reflective of the more distant future and more realistic precipitation projections are required to explore whether the active glacier can be sustained further into the future or will lose ice more rapidly than is found in this study. However, while future precipitation changes may be important for glacier volume change under RCP4.5, we do not expect a sufficient increase in precipitation beyond 2100 CE to compensate for the warming projected under RCP8.5.

Deleted: which

Deleted:

Deleted: (Benn and Lehmkuhl, 2000)

1286 of low frequency–high magnitude avalanche events on accumulation rates would be useful to refine
1287 this calculation but the contribution of avalanches to glacier accumulation over decadal time scales
1288 remains **extremely** challenging to measure (Purdie et al., 2025).

1290 4.2 Impacts of mesoscale and microscale meteorology on glacier change

1291 Our study addresses fine-scale temporal (hourly) and spatial (100 m) glacier surface processes,
1292 including avalanching and sublimation, that affect glacier surface mass balance across the elevation
1293 range of Khumbu Glacier, but further observations of meteorological and glaciological conditions at
1294 the highest elevations would be beneficial, and are needed if micro-scale processes are to be included
1295 in glacier models (Brun et al., 2023; Khadka et al., 2021; Mölg et al., 2014; Shaw et al., 2022). Analysis
1296 of meteorological observations from AWS across the Dudh Koshi catchment indicated that precipitation
1297 gradients were weak, slightly negative or absent, confirming the observations of Salerno et al. (2015)
1298 and Yang et al. (2017). To test the sensitivity of precipitation to elevation, COSIPY was forced by a
1299 gridded climate distributed using weak negative, weak positive, and no precipitation gradients
1300 distributed across the model domain using a linear regression with elevation from the 100-m resolution
1301 DEM. The results of these experiments were used to force iSOSIA and the simulated historical glacier
1302 evolution was similar, resulting in only a 10 m difference in the maximum ice thickness between
1303 simulations with different precipitation gradients (result not shown).

1305 The mass balance sensitivity to seasonal and daily variations in lapse rate showed a lesser impact on
1306 glacier-wide mass balance than in other studies, due to the large elevation range of Khumbu Glacier
1307 whereby a smaller fraction of the glacier relative to total area is located along the zero degree isotherm
1308 (e.g., compared to Yala Glacier in Nepal; Immerzeel et al., 2014). Seasonal and daily lapse rates that
1309 accounted for marked lower values during the monsoon season and at night gave a mean annual value
1310 of 5.54 °C km⁻¹, which produced glacier-wide mass balance and ice thickness simulations that were
1311 closest to geodetic observations and represented the maximum rates of surface lowering in the upper
1312 ablation area where the debris layer is thinnest (Fig. 3D and 3E).

1314 Sublimation simulated in our study occurred at all elevations with the highest rate of ice loss due to
1315 sublimation ($-0.12 \text{ m w.e. a}^{-1}$) in the upper reaches of the Khumbu Glacier catchment near to South Col
1316 (about 7,495 m a.s.l.) where sublimation dominated ablation with only minor seasonality (Fig. A6).
1317 Whilst this amount of ice loss by sublimation is not negligible, it is almost half that found in the point-
1318 based calculations after adjusting for the different time periods represented by our studies (Matthews et
1319 al., 2020), which is likely due to the assumed uniformity of wind speed across the model domain in
1320 COSIPY. Future work to improve the calculation of sublimation in distributed surface mass balance
1321 calculations for high-elevation glaciers would be valuable.

1323 While we have considered the effects of mesoscale meteorology on glacier mass balance, smaller-scale
1324 processes operating close to the land surface could also be important. Katabatic winds were suggested
1325 to explain a local 15-year decrease in maximum air temperatures and precipitation over glaciers while
1326 minimum air temperatures continued to rise (Salerno et al., 2023). However, this effect was found to be
1327 short-lived (Shaw et al., 2025) and the impact of microscale near-surface cooling on the duration and
1328 extent of mesoscale precipitation and accumulation is likely to be minimal and therefore unlikely to
1329 significantly affect glacier-wide mass balance (Mott et al., 2020; Shaw et al., 2024). Observations from
1330 the Camp 2 AWS (6,464 m a.s.l.) indicate that surface energy fluxes may be sufficient to cause non-
1331 negligible melting of glacier surfaces despite freezing air temperatures (Matthews et al., 2020). Results
1332 from an ice core from South Col Glacier (>8,000 m a.s.l.) combined with COSIPY experiments
1333 suggested that ablation may also take place at even at the highest elevations (Potocki et al., 2022).
1334 However, a subsequent study found no evidence of glacier mass change, and identified large
1335 uncertainties associated with simulating mass balance at these extreme elevations where sub-daily air
1336 temperature gradients and the duration of snow cover strongly affect ablation and accumulation (Brun
1337 et al., 2023). Future work is needed to reduce these uncertainties, as very few observations exist of
1338 accumulation processes and the upper limit of ablation processes for high-elevation Himalayan glaciers.

1340 4.3 Possible outcomes under RCP8.5

Moved down [7]: Our study addresses fine-scale temporal (hourly) and spatial (100 m) glacier surface processes, including avalanching and sublimation, that affect glacier surface mass balance across the elevation range of Khumbu Glacier, but further observations of meteorological and glaciological conditions at the highest elevations would be beneficial, and are needed if micro-scale processes are to be included in glacier models (Brun et al., 2023; Khadka et al., 2021; Mölg et al., 2014; Shaw et al., 2022).

Deleted: ¶

4.2 Comparison with outcomes under RCP8.5¶

Current global greenhouse gas emissions are following the trajectory of the intermediate emissions scenario RCP4.5, while the high emissions scenario RCP8.5 could be described as ‘low possibility but high impact’ (Pedersen et al., 2020). However, as represented in the RCMs used in our study, mountain regions are warming more rapidly than the global mean such that a global temperature rise of 1.5°C will lead to $2.1 \pm 0.1^\circ\text{C}$ of warming in High Mountain Asia (Kraaijenbrink et al., 2017; Pepin et al., 2022) although the occurrence of elevation-dependent warming above 5,000 m a.s.l. is debated (Gao et al., 2018). The high temperatures projected under RCP8.5 could potentially be offset partly by increased precipitation, given that high-magnitude precipitation events from winter Westerly disturbances increased by a factor of seven between present day and 2100 CE in the IPSL RCM under RCP8.5. However, we found no evidence of future increases in precipitation offsetting RCP8.5 warming; net glacier mass balance was strongly negative in all RCP8.5 experiments and insufficient to maintain any actively flowing glacier. Under RCP8.5, glacier mass balance in the monsoon-influenced Himalaya may therefore shift from being driven by accumulation during the monsoon to predominantly during winter. Monsoon precipitation would only result in snow accumulation at the very highest elevations and would be insufficient to maintain flowing glaciers. This outcome is avoidable by limiting anthropogenic warming to within RCP4.5, which, due to the associated increase in precipitation, could sustain nearly two thirds of the current glacier volume until 2100 CE and potentially for two centuries further into the future. ¶

Deleted: ¶

... [7]

Deleted: 3

Moved (insertion) [7]

Deleted: ¶

Deleted: -

Deleted: an

Deleted: on Khumbu Glacier

Deleted: exist

1391 Current global greenhouse gas emissions are following the trajectory of the intermediate emissions
1392 scenario RCP4.5, while the high emissions scenario RCP8.5 could be described as ‘low possibility but
1393 high impact’ (Pedersen et al., 2020). However, as represented in the RCMs used in our study, mountain
1394 regions are warming more rapidly than the global mean such that a global temperature rise of 1.5°C will
1395 lead to $2.1 \pm 0.1^\circ\text{C}$ of warming in High Mountain Asia (Kraaijenbrink et al., 2017; Pepin et al., 2022)
1396 although the occurrence of elevation-dependent warming above 5,000 m a.s.l. is debated (Gao et al.,
1397 2018). The high temperatures projected under RCP8.5 could potentially be offset partly by increased
1398 precipitation, given that high-magnitude precipitation events from winter Westerly disturbances
1399 increased by a factor of seven between present day and 2100 CE in the IPSL RCM under RCP8.5.

1400
1401 We found no evidence of future increases in precipitation offsetting RCP8.5 warming; net glacier mass
1402 balance was strongly negative in all RCP8.5 experiments and insufficient to maintain any actively
1403 flowing glacier. Under RCP8.5, glacier mass balance in the monsoon-influenced Himalaya may
1404 therefore shift from being driven by accumulation during the monsoon to predominantly during winter.
1405 Monsoon precipitation would only result in snow accumulation at the very highest elevations and would
1406 be insufficient to maintain flowing glaciers. This outcome is avoidable by limiting anthropogenic
1407 warming to within RCP4.5, which, due to the associated increase in precipitation, could sustain nearly
1408 two thirds of the current glacier volume until 2100 CE and potentially for two centuries further into the
1409 future.

1411 **4.4 Comparison with global glacier modelling results**

1412 A recent global glacier modelling study forced by an ensemble of 10 GCMs projected mass loss of 64%
1413 for Khumbu Glacier by 2100 CE (Rounce et al., 2023). In comparison, our experiments project less
1414 severe rates of decline, resulting in 30% less mass loss under the RCP4.5 future climate scenario than
1415 in the global study (Fig. 10C). One difference between these results is that rather than using the global
1416 glacier inventory outline to define the glacier margins we consider only the actively flowing glacier and
1417 so exclude 20% of the starting glacier volume in the detached tongue. We would expect the two sections
1418 of the glacier to evolve along different paths; while the active glacier responds to climate change as
1419 projected in our experiments, thick supraglacial debris mantling the detached tongue could allow this
1420 ice mass to survive and slowly decay *in situ* for many decades beyond the present day. The decay of the
1421 detached tongue may however increase due to erosion of the surface by ice cliffs and supraglacial water
1422 bodies that are expanding across the former glacier surface (King et al., 2020).

1423
1424 Our experiments only consider the rapidly changing active glacier, and we expect that the debris-
1425 covered tongue would melt more slowly than projected in the global modelling study, but as we do not
1426 consider the stagnant tongue to be part of the present-day glacier the ice volume simulated at the start
1427 of our experiments is smaller than that represented by Rounce et al. (2023) and other studies based on
1428 the RGI glacier inventory. The dynamically detached debris-covered tongue represents about 20% of
1429 the present-day glacier volume and contains ice estimated as up to 360 m thick. The mean present-day
1430 ablation rate across this section of the glacier simulated in Rowan et al. (2021) is $-0.54 \text{ m w.e. a}^{-1}$ which
1431 can be used to estimate the life expectancy of the debris-covered tongue assuming no input of ice from
1432 the active glacier and no change in ablation rate due to thickening of supraglacial debris or the
1433 development of ice cliffs and supraglacial ponds. While the thickest part of the detached tongue may
1434 survive for ~600 years, the mean life expectancy of this ice mass is 176 ± 148 years from the present
1435 day meaning that the former debris-covered tongue will vanish by 2200 CE.

1437 **4.5 The response of large debris-covered glaciers to climate change**

1438 The dynamic response time of large glaciers to climate change is of the order of centuries. For this
1439 reason, we start our simulations from the late Holocene (~1 ka) moraine extent when Khumbu Glacier
1440 was last considered dynamically stable (Hornsey et al., 2022; Rowan et al., 2015). The relationship
1441 between glacier response time and mass balance becomes less important after 2100 CE when the glacier
1442 is so small that ice flow has little impact on glacier volume change. Global and regional glacier
1443 modelling studies typically start their simulations in the current Century (e.g., 2000–2007 CE in
1444 Marzeion et al. (2020); 2015 CE in Rounce et al. (2023)) and a further complication arises from the use
1445 of global glacier inventories as a starting point for glacier modelling studies as such inventories cannot

Deleted: 4

Deleted: ;

Deleted: f

Deleted: c

1450 capture the current dynamic state of glaciers that are imbalanced, and include all ice-covered areas
1451 rather than identifying only actively flowing ice. However, satellite-derived velocity products could be
1452 used identify where ice flow within glacier outlines declines to negligible rates (Dehecq et al., 2019).

1453
1454 The RGI 7.0 inventory for Khumbu Glacier is based on imagery from 1999 CE (RGI 7.0 Consortium,
1455 2023) where the detached debris-covered tongue represents 20% of the glacier volume contained within
1456 this outline (Fig. 1C). Simulations that integrated the stagnant tongue into the model domain rather than
1457 as part of the flowing ice improved the representation of simulated ice flow compared to observed
1458 values, supporting our conclusion that the debris-covered tongue has been dynamically detached from
1459 the active glacier for 50–100 years (Rowan et al., 2021). Field observations support the concept of
1460 active and stagnant sections co-existing in contact with each other as englacial optical televising
1461 indicated that thrusting occurs at several sites, denoted by skewed internal debris layers and of basal ice
1462 that has been thrust to the glacier surface, near to the active glacier terminus from the direction of
1463 Khumbu Icefall (Miles et al., 2021). Our simulations show that development of supraglacial debris at
1464 the active glacier terminus reduced net volume loss by 13% (Fig. 8). Dynamic detachment of debris-
1465 covered tongues could allow these glaciers to move closer to equilibrium with a rapidly changing
1466 climate, the local mass balance gradient is a more important control on glacier change for both clean-
1467 ice glaciers and debris-covered Himalayan glaciers.

1468 5. Conclusions

1470 In the monsoon-influenced Himalaya, 85% of the glacier area is located higher than 5,000 m above sea
1471 level, and 21% of this ice is above 6000 m in elevation. Despite these high elevations, Himalayan
1472 glaciers are rapidly losing ice in response to recent warming and are projected to shrink by 53% to 70%
1473 during this Century. However, the impact of future changes in precipitation on glacier loss remains
1474 uncertain, because changes in precipitation amount and distribution is often overlooked in glacier model
1475 projections. We explored the effects of future warming in tandem with changes in precipitation by
1476 simulating the evolution of Khumbu Glacier in the Everest region of Nepal using a surface energy and
1477 mass balance model forced by downscaled Regional Climate Model outputs to drive an ice-dynamical
1478 glacier evolution model. Historical warming commits Khumbu Glacier to loss of 10–23% of the total
1479 ice volume by 2100 CE. While warming due to intermediate future greenhouse gas emissions (RCP4.5)
1480 will lead to glacier volume loss of 70% by 2100 CE, the projected concurrent increase in precipitation
1481 amount will offset 34% of this and so reduce glacier loss by about a half. However, high future
1482 emissions (RCP8.5) will not be compensated by changes in precipitation amount but will instead result
1483 in substantial ablation above 6,000 m with devastating consequences for one of the highest glaciers on
1484 Earth. Our results indicate that the net mass balance of Khumbu Glacier could be close to zero in 2100
1485 CE under RCP4.5 and therefore, if climate change is limited to this intermediate emissions scenario,
1486 Khumbu Glacier will recede to the base of the icefall with insignificant further change in glacier volume
1487 beyond this point. In this scenario, Khumbu Glacier has a similar extent in 2100 CE to the active section
1488 of the present-day glacier, and represents at least one example of how monsoon-influenced Himalayan
1489 glaciers could persist into the future if global efforts are sufficient to mitigate anthropogenic climate
1490 change.

1491
1492
1493

Deleted: c

Deleted: (Fig. 1c)

Deleted: .

Deleted: c

Deleted: mesoscale meteorology

Deleted: not often

Deleted: represented

Deleted: —a benchmark glacier in the monsoon-influenced
Nepal Himalaya—

Deleted: mesoscale glacier

Deleted: ling

1505 **Code availability**
 1506 The COSIPY version 1.3 glacier surface energy and mass balance model is available from the original
 1507 publication describing this model (Sauter et al., 2020) and Zenodo (Arndt et al., 2020). The iSOSIA
 1508 version spm-3.3.3r glacier model is available from Zenodo (Rowan and Pedersen, 2024).
 1509

1510 **Data availability**
 1511 Daily data from the Coordinated Regional Downscaling Experiment (CORDEX) South Asia domain
 1512 were downloaded from the Indian Institute of Tropical Meteorology website
 1513 (http://cccr.tropmet.res.in/home/cordexsa_about.jsp) for the grid box nearest to Khumbu Glacier
 1514 (27.9065°N, 86.4353°E). Incoming shortwave and longwave radiation components were downloaded
 1515 from the ESGF portal (<https://esgf-ui.ceda.ac.uk/cog/projects/cordex-ceda/>). Meteorological
 1516 observations were derived from the Ev-K2-CNR SHARE network (<https://www.ev-k2cnr.org>) and the
 1517 GlacioClim (<https://glacioclim.osug.fr/>).
 1518

1519 **Author contributions**
 1520 Conceptualisation: DJQ, ANR, AVR
 1521 Data curation: ASD, ANR, AVR
 1522 Formal analysis: ASD, ANR, AVR
 1523 Funding acquisition: DJQ, ANR, AVR
 1524 Investigation: ASD
 1525 Methodology: ASD, ANR, AVR, VKP
 1526 Project administration: DJQ, ANR
 1527 Resources: DJQ, ANR
 1528 Software: AVR, VKP
 1529 Supervision: DJQ, ANR, AVR
 1530 Validation: ASD, AVR
 1531 Visualisation: ASD, AVR
 1532 Writing – original draft preparation: ASD, AVR, DJQ, ANR, VKP
 1533 Writing – review and editing: ASD, AVR, DJQ, ANR, VKP
 1534

1535 **Competing interests**
 1536 The authors declare that they have no conflicts of interest [related to this work](#).
 1537

1538 **Acknowledgements**
 1539 Tobias Sauter and Anselm Arndt are thanked for support in using COSIPY. We thank Patrick Wagon
 1540 for sharing the Pyramid and Changri Nup Glacier automatic weather station data. We thank David
 1541 Rounce for sharing [the global glacier model results for Khumbu Glacier from Rounce et al. \(2023\)](#). [We](#)
 1542 [thank Editor Emily Collier, Emily Potter and an anonymous reviewer for their detailed and constructive](#)
 1543 [comments that greatly improved the focus and clarity of this work](#).
 1544

1545 **Financial support**
 1546 ASD was supported by the Priestley International Centre for Climate at the University of Leeds, and a
 1547 University of Leeds Anniversary Research Scholarship. AVR was supported by a Royal Society
 1548 Dorothy Hodgkin Research Fellowship (DHF\R1\201113). [Some of the simulations presented were](#)
 1549 [performed using resources provided by Sigma2, the National Infrastructure for High-Performance](#)
 1550 [Computing and Data Storage in Norway](#).
 1551

1552 **References**
 1553
 1554 Altna, B. and Käab, A.: Ensemble matching of repeat satellite images applied to measure fast-changing
 1555 ice flow, verified with mountain climber trajectories on Khumbu icefall, Mount Everest, *J.*
 1556 *Glaciol.*, 66, 905–915, <https://doi.org/10.1017/jog.2020.66>, 2020.
 1557 Arndt, A., Sauter, T., Saß, B. (2020). cryotools/cosipy: COSIPY v1.3 – An open-source coupled
 1558 snowpack and ice surface energy and mass balance model (v1.3). Zenodo.
 1559 <https://doi.org/10.5281/zenodo.3902191>

- Deleted: 14 years of
- Deleted: m
- Deleted: the two Pyramid AWS at 5,050 m a.s.l. and at 5,035 m a.s.l. (
- Deleted: Ev-K2-CNR;
- Formatted: Font colour: Hyperlink
- Field Code Changed
- Deleted: West Changri Nup glacier AWS at 5,363 m a.s.l. (
- Deleted: :
- Formatted: Font colour: Hyperlink
- Field Code Changed

Moved down [2]: Some of the simulations presented were performed on resources provided by Sigma2, the National Infrastructure for High-Performance Computing and Data Storage in Norway.

Moved (insertion) [2]

Deleted: on

- 1572 Anderson, L. S. and Anderson, R. S.: Modeling debris-covered glaciers: response to steady debris
1573 deposition, *The Cryosphere*, 10, 1105–1124, <https://doi.org/10.5194/tc-10-1105-2016>, 2016.
- 1574 Bartlett, O. T., Ng, F. S. L., and Rowan, A. V.: Morphology and evolution of supraglacial hummocks on
1575 debris-covered Himalayan glaciers, *Earth Surf. Process. Landforms*, 46, 525–539,
1576 <https://doi.org/10.1002/esp.5043>, 2021.
- 1577 Benn, D. I. and Lehmkuhl, F.: Mass balance and equilibrium-line altitudes of glaciers in high-mountain
1578 environments, *Quaternary International*, 65–66, 15–29, [https://doi.org/10.1016/S1040-6182\(99\)00034-8](https://doi.org/10.1016/S1040-6182(99)00034-8), 2000.
- 1580 Benn, D. I. and Owen, L. A.: The role of the Indian summer monsoon and the mid-latitude westerlies
1581 in Himalayan glaciation: review and speculative discussion, *Journal of the Geological Society*,
1582 155, 353–363, <https://doi.org/10.1144/gsjgs.155.2.0353>, 1998.
- 1583 ~~Biemans, L.H. Speelman, F. Ludwig, E.J. Moors, A.J. Wiltshire, P. Kumar, D. Gerten, P. Kabat (2013)~~
1584 ~~Future water resources for food production in five South Asian river basins and potential for~~
1585 ~~adaptation—A modeling study, *Science of The Total Environment*,~~
1586 ~~<https://doi.org/10.1016/j.scitotenv.2013.05.092>.~~
- 1587 Bonekamp, P. N. J., Wanders, N., Wiel, K., Lutz, A. F., and Immerzeel, W. W.: Using large ensemble
1588 modelling to derive future changes in mountain specific climate indicators in a 2 and 3°C warmer
1589 world in High Mountain Asia, *Int J Climatol*, 41, <https://doi.org/10.1002/joc.6742>, 2021.
- 1590 Bookhagen, B. and Burbank, D. W.: Topography, relief, and TRMM-derived rainfall variations along
1591 the Himalaya, *Geophys. Res. Lett.*, 33, L08405, <https://doi.org/10.1029/2006GL026037>, 2006.
- 1592 Brock, B.W., Willis, I.C. and Sharp, M.J., 2006. Measurement and parameterization of aerodynamic
1593 roughness length variations at Haut Glacier d’Arolla, Switzerland. *Journal of Glaciology*,
1594 52(177), pp.281-297. <https://doi.org/10.3189/172756506781828746>
- 1595 Brun, F., King, O., Réveillet, M., Amory, C., Planchot, A., Berthier, E., Dehecq, A., Bolch, T., Fourteau,
1596 K., Brondex, J., Dumont, M., Mayer, C., Leinss, S., Hugonnet, R., and Wagnon, P.: Everest South
1597 Col Glacier did not thin during the period 1984–2017, *The Cryosphere*, 17, 3251–3268,
1598 <https://doi.org/10.5194/tc-17-3251-2023>, 2023.
- 1599 Collins, M., Knutti, R., and Arblaster, J.: Long-term Climate Change: Projections, Commitments and
1600 Irreversibility. In: *Climate Change 2013: The Physical Science Basis. Contribution of Working*
1601 *Group I to the Fifth Assessment Report of the Intergovernmental Panel on Climate Change*
1602 [Stocker, T.F., D. Qin, G.-K. Plattner, M. Tignor, S.K. Allen, J. Boschung, A. Nauels, Y. Xia, V.
1603 Bex and P.M. Midgley (eds.)]. Cambridge University Press, Cambridge, United Kingdom and
1604 New York, NY, USA., 1–108., 2013.
- 1605 Compagno, L., Huss, M., Miles, E. S., McCarthy, M. J., Zekollari, H., Dehecq, A., Pellicciotti, F., and
1606 Farinotti, D.: Modelling supraglacial debris-cover evolution from the single-glacier to the
1607 regional scale: an application to High Mountain Asia, *The Cryosphere*, 16, 1697–1718,
1608 <https://doi.org/10.5194/tc-16-1697-2022>, 2022.
- 1609 Cuffey, K.M. and Paterson, W.S.B., 2010. *The physics of glaciers*. Academic Press.
- 1610 Dehecq, A., Gourmelen, N., Gardner, A. S., Brun, F., Goldberg, D., Nienow, P. W., Berthier, E., Vincent,
1611 C., Wagnon, P., and Trouvé, E.: Twenty-first century glacier slowdown driven by mass loss in
1612 High Mountain Asia, *Nature Geosci*, 12, 22–27, <https://doi.org/10.1038/s41561-018-0271-9>,
1613 2019.
- 1614 Egholm, D. L., Knudsen, M. F., Clark, C. D., and Lesemann, J. E.: Modeling the flow of glaciers in
1615 steep terrains: The integrated second-order shallow ice approximation (iSOSIA), *J. Geophys.*
1616 *Res.*, 116, <https://doi.org/10.1029/2010JF001900>, 2011.
- 1617 Farinotti, D., Huss, M., Fürst, J. J., Landmann, J., Machguth, H., Maussion, F., and Pandit, A.: A
1618 consensus estimate for the ice thickness distribution of all glaciers on Earth, *Nat. Geosci.*, 12,
1619 168–173, <https://doi.org/10.1038/s41561-019-0300-3>, 2019.
- 1620 Farr, T. G., Rosen, P. A., Caro, E., Crippen, R., Duren, R., Hensley, S., Kobrick, M., Paller, M.,
1621 Rodriguez, E., Roth, L., Seal, D., Shaffer, S., Shimada, J., Umland, J., Werner, M., Oskin, M.,
1622 Burbank, D., and Alsdorf, D.: The Shuttle Radar Topography Mission, *Reviews of Geophysics*,
1623 45, 2005RG000183, <https://doi.org/10.1029/2005RG000183>, 2007.
- 1624 Ferguson, J. and Vieli, A.: Modelling steady states and the transient response of debris-covered glaciers,
1625 *Cryosphere*, <https://doi.org/10.5194/tc-2020-228>, 2020.

Deleted: H.

- 1627 Förster, K., Hanzer, F., Winter, B., Marke, T., and Strasser, U.: An open-source MEteoroLOGical
 1628 observation time series DISaggregation Tool (MELODIST v0.1.1), *Geosci. Model Dev.*, 9, 2315–
 1629 2333, <https://doi.org/10.5194/gmd-9-2315-2016>, 2016.
- 1630 Gades, A., Conway, H., Nereson, N., Naito, N., and Kadota, T.: Radio echo-sounding through
 1631 supraglacial debris on Lirung and Khumbu Glaciers, Nepal Himalayas, *Debris-Covered Glaciers*
 1632 (Proceedings of a workshop held at Seattle, Washington, USA, September 2000). IAHS, 264, 13–
 1633 22, 2000.
- 1634 Gao, Y., Chen, F., Lettenmaier, D. P., Xu, J., Xiao, L., and Li, X.: Does elevation-dependent warming
 1635 hold true above 5000 m elevation? Lessons from the Tibetan Plateau, *npj Clim Atmos Sci*, 1, 19,
 1636 <https://doi.org/10.1038/s41612-018-0030-z>, 2018.
- 1637 Gromke, C., Manes, C., Walter, B., Lehning, M. and Guala, M., 2011. Aerodynamic roughness length
 1638 of fresh snow. *Boundary-Layer Meteorology*, 141, pp.21-34. [https://doi.org/10.1007/s10546-](https://doi.org/10.1007/s10546-011-9623-3)
 1639 [011-9623-3](https://doi.org/10.1007/s10546-011-9623-3)
- 1640 Guo, S., Chen, R., Liu, G., Han, C., Song, Y., Liu, J., Yang, Y., Liu, Z., Wang, X., Liu, X. and Wang, L.,
 1641 2018. Simple parameterization of aerodynamic roughness lengths and the turbulent heat fluxes
 1642 at the top of midlatitude August-One Glacier, Qilian Mountains, China. *Journal of Geophysical*
 1643 *Research: Atmospheres*, 123(21), pp.12-066. <https://doi.org/10.1029/2018JD028875>
- 1644 Herreid, S. and Pellicciotti, F.: The state of rock debris covering Earth’s glaciers, *Nat. Geosci.*, 13, 621–
 1645 627, <https://doi.org/10.1038/s41561-020-0615-0>, 2020.
- 1646 Hornsey, J., Rowan, A. V., Kirkbride, M. P., Livingstone, S. J., Fabel, D., Rodes, A., Quincey, D. J.,
 1647 Hubbard, B., and Jomelli, V.: Be-10 Dating of Ice-Marginal Moraines in the Khumbu Valley,
 1648 Nepal, Central Himalaya, Reveals the Response of Monsoon-Influenced Glaciers to Holocene
 1649 Climate Change, *JGR Earth Surface*, 127, <https://doi.org/10.1029/2022JF006645>, 2022.
- 1650 Huintjes, E., Neckel, N., Hochschild, V., and Schneider, C.: Surface energy and mass balance at
 1651 Purogangri ice cap, central Tibetan Plateau, 2001–2011, *J. Glaciol.*, 61, 1048–1060,
 1652 <https://doi.org/10.3189/2015JG15J056>, 2015.
- 1653 Immerzeel, W. W., van Beek, L. P. H., Konz, M., Shrestha, A. B., and Bierkens, M. F. P.: Hydrological
 1654 response to climate change in a glacierized catchment in the Himalayas, *Climatic Change*, 110,
 1655 721–736, <https://doi.org/10.1007/s10584-011-0143-4>, 2012.
- 1656 Irvine-Fynn, T.D., Sanz-Ablanedo, E., Rutter, N., Smith, M.W. and Chandler, J.H., 2014. Measuring
 1657 glacier surface roughness using plot-scale, close-range digital photogrammetry. *Journal of*
 1658 *Glaciology*, 60(223), pp.957-969. doi:10.3189/2014JoG14J032
- 1659 Jouvett, G., Huss, M., Funk, M., and Blatter, H.: Modelling the retreat of Grosser Aletschgletscher,
 1660 Switzerland, in a changing climate, *J. Glaciol.*, 57, 1033–1045,
 1661 <https://doi.org/10.3189/002214311798843359>, 2011.
- 1662 Kaini, S., Nepal, S., Pradhananga, S., Gardner, T. and Sharma, A. K. (2019) Representative general
 1663 circulation models selection and downscaling of climate data for the transboundary Koshi river
 1664 basin in China and Nepal. *International Journal of Climatology*, 40(9): 4131-4149. doi:
 1665 10.1002/joc.6447.
- 1666 Katzenberger, A., Schewe, J., Pongratz, J., and Levermann, A.: Robust increase of Indian monsoon
 1667 rainfall and its variability under future warming in CMIP6 models, *Earth Syst. Dynam.*, 12, 367–
 1668 386, <https://doi.org/10.5194/esd-12-367-2021>, 2021.
- 1669 Khadka, A., Matthews, T., Perry, L. B., Koch, I., Wagnon, P., Shrestha, D., Sherpa, T. C., Aryal, D., Tait,
 1670 A., Sherpa, T. G., Tuladhar, S., Baidya, S. K., Elvin, S., Elmore, A. C., Gajurel, A., and Mayewski,
 1671 P. A.: Weather On MOUNT EVEREST During The 2019 Summer MONSOON, *Weather*, 76, 205–
 1672 207, <https://doi.org/10.1002/wea.3931>, 2021.
- 1673 King, O., Bhattacharya, A., Ghuffar, S., Tait, A., Guilford, S., Elmore, A. C., and Bolch, T.: Six Decades
 1674 of Glacier Mass Changes around Mt. Everest Are Revealed by Historical and Contemporary
 1675 Images, *One Earth*, 3, 608–620, <https://doi.org/10.1016/j.oneear.2020.10.019>, 2020.
- 1676 Knap, W.H. and Oerlemans, J., 1996. The surface albedo of the Greenland ice sheet: satellite-derived
 1677 and in situ measurements in the Søndre Strømfjord area during the 1991 melt season. *Journal of*
 1678 *Glaciology*, 42(141), pp.364-374. doi:10.3189/S0022143000004214
- 1679 [Kneib, M., Maussion, F., Brun, F., Carcanade, G., Farinotti, D., Huss, M., Van Tiel, M., Jouberton, A.,](#)
 1680 [Schmitt, P., Schuster, L., Dehecq, A., and Champollion, N.: Topographically-controlled](#)

1681 [contribution of avalanches to glacier mass balance in the 21st century, Nat Commun, 16, 10122,](https://doi.org/10.1038/s41467-025-65608-z)
1682 [https://doi.org/10.1038/s41467-025-65608-z, 2025.](https://doi.org/10.1038/s41467-025-65608-z)

1683 Kraaijenbrink, P. D. A., Bierkens, M. F. P., Lutz, A. F., and Immerzeel, W. W.: Impact of a global
1684 temperature rise of 1.5 degrees Celsius on Asia's glaciers, *Nature*, 549, 257–260,
1685 <https://doi.org/10.1038/nature23878>, 2017.

1686 Lafon, T., Dadson, S., Buys, G. and Prudhomme, C., 2013. Bias correction of daily precipitation
1687 simulated by a regional climate model: a comparison of methods. *International journal of*
1688 *climatology*, 33(6), pp.1367-1381.

1689 [Laha, S., Kumari, R., Singh, S., Mishra, A., Sharma, T., Banerjee, A., Nainwal, H. C., and Shankar, R.:
1690 Evaluating the contribution of avalanching to the mass balance of Himalayan glaciers, *Ann.*
1691 *Glaciol.*, 58, 110–118, <https://doi.org/10.1017/aog.2017.27>, 2017.](https://doi.org/10.1017/aog.2017.27)

1692 Luo, M., Liu, T., Meng, F., Duan, Y., Frankl, A., Bao, A. and De Maeyer, P. 2018. Comparing bias
1693 correction methods used in downscaling precipitation and temperature from regional climate
1694 models: A case study from the Kaidu River basin in western China. *Water*. 10(8), pp. 1046.
1695 <https://doi.org/10.3390/w10081046>

1696 Lutz, A.F., Immerzeel, W.W., Kraaijenbrink, P.D., Shrestha, A.B. and Bierkens, M.F., 2016. Climate
1697 change impacts on the upper Indus hydrology: sources, shifts and extremes. *PloS one*, 11(11),
1698 p.e0165630.

1699 Marzeion, B., Hock, R., Anderson, B., Bliss, A., Champollion, N., Fujita, K., Huss, M., Immerzeel, W.
1700 W., Kraaijenbrink, P., Malles, J., Maussion, F., Radić, V., Rounce, D. R., Sakai, A., Shannon, S.,
1701 Van De Wal, R., and Zekollari, H.: Partitioning the Uncertainty of Ensemble Projections of
1702 Global Glacier Mass Change, *Earth's Future*, 8, e2019EF001470,
1703 <https://doi.org/10.1029/2019EF001470>, 2020.

1704 Maraun, D., 2016. Bias correcting climate change simulations-a critical review. *Current Climate*
1705 *Change Reports*, 2(4), pp.211-220.

1706 Matthews, T., Perry, L. B., Koch, I., Aryal, D., Khadka, A., Shrestha, D., Abernathy, K., Elmore, A. C.,
1707 Seimon, A., Tait, A., Elvin, S., Tuladhar, S., Baidya, S. K., Potocki, M., Birkel, S. D., Kang, S.,
1708 Sherpa, T. C., Gajurel, A., and Mayewski, P. A.: Going to Extremes: Installing the World's
1709 Highest Weather Stations on Mount Everest, *Bulletin of the American Meteorological Society*,
1710 101, E1870–E1890, <https://doi.org/10.1175/BAMS-D-19-0198.1>, 2020.

1711 Maurer, J. M., Schaefer, J. M., Rupper, S., and Corley, A.: Acceleration of ice loss across the Himalayas
1712 over the past 40 years, *Sci. Adv.*, 5, eaav7266, <https://doi.org/10.1126/sciadv.aav7266>, 2019.

1713 Miles, E. S., Willis, I., Buri, P., Steiner, J. F., Arnold, N. S., and Pellicciotti, F.: Surface Pond Energy
1714 Absorption Across Four Himalayan Glaciers Accounts for 1/8 of Total Catchment Ice Loss,
1715 *Geophys. Res. Lett.*, 45, <https://doi.org/10.1029/2018GL079678>, 2018a.

1716 Miles, K. E., Hubbard, B., Quincey, D. J., Miles, E. S., Sherpa, T. C., Rowan, A. V., and Doyle, S. H.:
1717 Polythermal structure of a Himalayan debris-covered glacier revealed by borehole thermometry,
1718 *Sci Rep*, 8, 16825, <https://doi.org/10.1038/s41598-018-34327-5>, 2018b.

1719 Miles, K. E., Hubbard, B., Miles, E. S., Quincey, D. J., Rowan, A. V., Kirkbride, M., and Hornsey, J.:
1720 Continuous borehole optical televiewing reveals variable englacial debris concentrations at
1721 Khumbu Glacier, Nepal, *Commun Earth Environ*, 2, 12, [https://doi.org/10.1038/s43247-020-](https://doi.org/10.1038/s43247-020-00070-x)
1722 [00070-x](https://doi.org/10.1038/s43247-020-00070-x), 2021.

1723 [Miles, K. E., Hubbard, B., Miles, E. S., Quincey, D. J., and Rowan, A. V.: Internal structure of a
1724 Himalayan debris-covered glacier revealed by borehole optical televiewing, *J. Glaciol.*, 1–12,
1725 <https://doi.org/10.1017/jog.2022.100>, 2022.](https://doi.org/10.1017/jog.2022.100)

1726 Mölg, T., Maussion, F., Yang, W. and Scherer, D., 2012. The footprint of Asian monsoon dynamics in
1727 the mass and energy balance of a Tibetan glacier. *The Cryosphere*, 6(6), pp.1445-1461.
1728 <https://doi.org/10.5194/tc-6-1445-2012>

1729 Mölg, T., Maussion, F., and Scherer, D.: Mid-latitude westerlies as a driver of glacier variability in
1730 monsoonal High Asia, *Nature Clim Change*, 4, 68–73, <https://doi.org/10.1038/nclimate2055>,
1731 2014.

1732 Mott, R., Stiperski, I., and Nicholson, L.: Spatio-temporal flow variations driving heat exchange
1733 processes at a mountain glacier, *The Cryosphere*, 14, 4699–4718, [https://doi.org/10.5194/tc-14-](https://doi.org/10.5194/tc-14-4699-2020)
1734 [4699-2020](https://doi.org/10.5194/tc-14-4699-2020), 2020.

Deleted: 1

1736 Nakawo, M.: Processes Which Distribute Supraglacial Debris On The Khumbu Glacier, Nepal
1737 Himalaya, *Annals of Glaciology*, 8, 1986.

1738 Nicholson, L., Wirbel, A., Mayer, C., and Lambrecht, A.: The Challenge of Non-Stationary Feedbacks
1739 in Modeling the Response of Debris-Covered Glaciers to Climate Forcing, *Front. Earth Sci.*, 9,
1740 662695, <https://doi.org/10.3389/feart.2021.662695>, 2021.

1741 Oerlemans, J., 2001. *Glaciers and climate change*. CRC Press.

1742 Owen, L. A., Robinson, R., Benn, D. I., Finkel, R. C., Davis, N. K., Yi, C., Putkonen, J., Li, D., and
1743 Murray, A. S.: Quaternary glaciation of Mount Everest, *Quaternary Science Reviews*, 28, 1412–
1744 1433, <https://doi.org/10.1016/j.quascirev.2009.02.010>, 2009.

1745 Pedersen, J. S. T., Van Vuuren, D. P., Aparicio, B. A., Swart, R., Gupta, J., and Santos, F. D.: Variability
1746 in historical emissions trends suggests a need for a wide range of global scenarios and regional
1747 analyses, *Commun Earth Environ*, 1, 41, <https://doi.org/10.1038/s43247-020-00045-y>, 2020.

1748 Pellicciotti, F., Stephan, C., Miles, E., Herreid, S., Immerzeel, W. W., and Bolch, T.: Mass-balance
1749 changes of the debris-covered glaciers in the Langtang Himal, Nepal, from 1974 to 1999, *J.*
1750 *Glaciol.*, 61, 373–386, <https://doi.org/10.3189/2015JG13J237>, 2015.

1751 Pepin, N. C., Arnone, E., Gobiet, A., Haslinger, K., Kotlarski, S., Notarnicola, C., Palazzi, E., Seibert,
1752 P., Serafin, S., Schöner, W., Terzago, S., Thornton, J. M., Vuille, M., and Adler, C.: Climate
1753 Changes and Their Elevational Patterns in the Mountains of the World, *Reviews of Geophysics*,
1754 60, <https://doi.org/10.1029/2020RG000730>, 2022.

1755 Piani, C., Weedon, G.P., Best, M., Gomes, S.M., Viterbo, P., Hagemann, S. and Haerter, J.O., 2010.
1756 Statistical bias correction of global simulated daily precipitation and temperature for the
1757 application of hydrological models. *Journal of hydrology*, 395(3-4), pp.199-215.
1758 <https://doi.org/10.1016/j.jhydrol.2010.10.024>

1759 Pierce, D. W., Barnett, T. P., Santer, B. D., and Gleckler, P. J.: Selecting global climate models for
1760 regional climate change studies, *Proc. Natl. Acad. Sci. U.S.A.*, 106, 8441–8446,
1761 <https://doi.org/10.1073/pnas.0900094106>, 2009.

1762 Potocki, M., Mayewski, P. A., Matthews, T., Perry, L. B., Schwikowski, M., Tait, A. M., Korotkikh, E.,
1763 Clifford, H., Kang, S., Sherpa, T. C., Singh, P. K., Koch, I., and Birkel, S.: Mt. Everest's highest
1764 glacier is a sentinel for accelerating ice loss, *npj Clim Atmos Sci*, 5, 7,
1765 <https://doi.org/10.1038/s41612-022-00230-0>, 2022.

1766 Pritchard, H. D.: Asia's shrinking glaciers protect large populations from drought stress, *Nature*, 569,
1767 649–654, <https://doi.org/10.1038/s41586-019-1240-1>, 2019.

1768 [Purdie, H., Kerr, T., Robson, B., Anderson, B., Lorrey, A. M., Rack, W., Brasington, J., and Bealing, P.:
1769 Mass balance characteristics of the 'vanishing' Rolleston Glacier, New Zealand, *Ann. Glaciol.*,
1770 66, e31, <https://doi.org/10.1017/aog.2025.10032>, 2025.](https://doi.org/10.1017/aog.2025.10032)

1771 Quincey, D. J., Luckman, A., and Benn, D.: Quantification of Everest region glacier velocities between
1772 1992 and 2002, using satellite radar interferometry and feature tracking, *J. Glaciol.*, 55, 596–606,
1773 <https://doi.org/10.3189/002214309789470987>, 2009.

1774 Ragettli, S., Immerzeel, W. W., and Pellicciotti, F.: Contrasting climate change impact on river flows
1775 from high-altitude catchments in the Himalayan and Andes Mountains, *Proc Natl Acad Sci USA*,
1776 113, 9222–9227, <https://doi.org/10.1073/pnas.1606526113>, 2016.

1777 RGI 7.0 Consortium: A Dataset of Global Glacier Outlines, Version 7.0. Boulder, Colorado USA.
1778 NSIDC: National Snow and Ice Data Center, <https://doi.org/10.5067/f6jmovy5navz>, 2023.

1779 Reiter, P., Gutjahr, O., Schefczyk, L., Heinemann, G. and Casper, M., 2018. Does applying quantile
1780 mapping to subsamples improve the bias correction of daily precipitation?. *International Journal*
1781 *of Climatology*, 38(4), pp.1623-1633.

1782 Roering, J. J., Kirchner, J. W., and Dietrich, W. E.: Evidence for nonlinear, diffusive sediment transport
1783 on hillslopes and implications for landscape morphology, *Water Resources Research*, 35, 853–
1784 870, <https://doi.org/10.1029/1998WR900090>, 1999.

1785 Rounce, D. R., Hock, R., Maussion, F., Hugonnet, R., Kochtitzky, W., Huss, M., Berthier, E.,
1786 Brinkerhoff, D., Compagno, L., Copland, L., Farinotti, D., Menounos, B., and McNabb, R. W.:
1787 Global glacier change in the 21st century: Every increase in temperature matters, *Science*, 379,
1788 78–83, <https://doi.org/10.1126/science.abo1324>, 2023.

1789 Rowan, A. V.: The ‘Little Ice Age’ in the Himalaya: A review of glacier advance driven by Northern
1790 Hemisphere temperature change, *The Holocene*, 27, 292–308,
1791 <https://doi.org/10.1177/0959683616658530>, 2017.

1792 Rowan, A. V., Egholm, D. L., Quincey, D. J., and Glasser, N. F.: Modelling the feedbacks between mass
1793 balance, ice flow and debris transport to predict the response to climate change of debris-covered
1794 glaciers in the Himalaya, *Earth and Planetary Science Letters*, 430, 427–438,
1795 <https://doi.org/10.1016/j.epsl.2015.09.004>, 2015.

1796 Rowan, A. V., Egholm, D. L., Quincey, D. J., Hubbard, B., King, O., Miles, E. S., Miles, K. E., and
1797 Hornsey, J.: The Role of Differential Ablation and Dynamic Detachment in Driving Accelerating
1798 Mass Loss From a Debris-Covered Himalayan Glacier, *J. Geophys. Res. Earth Surf.*, 126,
1799 <https://doi.org/10.1029/2020JF005761>, 2021.

1800 Rowan, A., & Pedersen, V. K. (2024). *annvrowan/isosia: iSOSIA version used in Schlich-Davies et al.*
1801 *(spm-3.3.3r)*. Zenodo. <https://doi.org/10.5281/zenodo.12666864>

1802 Salerno, F., Guyennon, N., Yang, K., Shaw, T. E., Lin, C., Colombo, N., Romano, E., Gruber, S., Bolch,
1803 T., Alessandri, A., Cristofanelli, P., Putero, D., Diolaiuti, G., Tartari, G., Verza, G., Thakuri, S.,
1804 Balsamo, G., Miles, E. S., and Pellicciotti, F.: Local cooling and drying induced by Himalayan
1805 glaciers under global warming, *Nat. Geosci.*, 16, 1120–1127, [https://doi.org/10.1038/s41561-](https://doi.org/10.1038/s41561-023-01331-y)
1806 [023-01331-y](https://doi.org/10.1038/s41561-023-01331-y), 2023.

1807 Sanjay, J., Krishnan, R., Shrestha, A. B., Rajbhandari, R., and Ren, G.-Y.: Downscaled climate change
1808 projections for the Hindu Kush Himalayan region using CORDEX South Asia regional climate
1809 models, *Advances in Climate Change Research*, 8, 185–198,
1810 <https://doi.org/10.1016/j.accre.2017.08.003>, 2017.

1811 Sauter, T., Arndt, A., and Schneider, C.: COSIPY v1.3 – an open-source coupled snowpack and ice
1812 surface energy and mass balance model, *Geosci. Model Dev.*, 13, 5645–5662,
1813 <https://doi.org/10.5194/gmd-13-5645-2020>, 2020.

1814 Shaw, T. E., Miles, E. S., Chen, D., Jouberton, A., Kneib, M., Fugger, S., Ou, T., Lai, H.-W., Fujita, K.,
1815 Yang, W., Fatichi, S., and Pellicciotti, F.: Multi-decadal monsoon characteristics and glacier
1816 response in High Mountain Asia, *Environ. Res. Lett.*, 17, 104001, [https://doi.org/10.1088/1748-](https://doi.org/10.1088/1748-9326/ac9008)
1817 [9326/ac9008](https://doi.org/10.1088/1748-9326/ac9008), 2022.

1818 Shaw, T. E., Buri, P., McCarthy, M., Miles, E. S., and Pellicciotti, F.: Local Controls on Near-Surface
1819 Glacier Cooling Under Warm Atmospheric Conditions, *JGR Atmospheres*, 129, e2023JD040214,
1820 <https://doi.org/10.1029/2023JD040214>, 2024.

1821 [Shaw, T. E., Miles, E. S., McCarthy, M., Buri, P., Guyennon, N., Salerno, F., Carturan, L., Brock, B.,](https://doi.org/10.1038/s41558-025-02449-0)
1822 [and Pellicciotti, F.: Mountain glaciers recouple to atmospheric warming over the twenty-first](https://doi.org/10.1038/s41558-025-02449-0)
1823 [century. *Nat. Clim. Chang.*, 15, 1212–1218, <https://doi.org/10.1038/s41558-025-02449-0>, 2025.](https://doi.org/10.1038/s41558-025-02449-0)

1824 Shea, J. M., Immerzeel, W. W., Wagnon, P., Vincent, C., and Bajracharya, S.: Modelling glacier change
1825 in the Everest region, Nepal Himalaya, *The Cryosphere*, 9, 1105–1128,
1826 <https://doi.org/10.5194/tc-9-1105-2015>, 2015.

1827 Sherpa, S. F., Wagnon, P., Brun, F., Berthier, E., Vincent, C., Lejeune, Y., et al. (2017). Contrasted
1828 surface mass balances of debris-free glaciers observed between the southern and the inner parts
1829 of the Everest region (2007–15). *Journal of Glaciology*, 63(240), 637–651.
1830 <https://doi.org/10.1017/jog.2017.30>

1831 Strickland, R. M., Covington, M. D., Gulley, J. D., Kayastha, R. B., and Blackstock, J. M.: Englacial
1832 Drainage Drives Positive Feedback Depression Growth on the Debris-Covered Ngozumpa
1833 Glacier, Nepal, *Geophysical Research Letters*, 50, e2023GL104389,
1834 <https://doi.org/10.1029/2023GL104389>, 2023.

1835 Vacco, D. A., Alley, R. B., and Pollard, D.: Glacial advance and stagnation caused by rock avalanches,
1836 *Earth and Planetary Science Letters*, 294, 123–130, <https://doi.org/10.1016/j.epsl.2010.03.019>,
1837 2010.

1838 Wagnon, P., Lafaysse, M., Lejeune, Y., Maisincho, L., Rojas, M. and Chazarin, J.P., 2009.
1839 Understanding and modeling the physical processes that govern the melting of snow cover in a
1840 tropical mountain environment in Ecuador. *Journal of Geophysical Research: Atmospheres*,
1841 114(D19).

1842 Watson, C. S., Quincey, D. J., Smith, M. W., Carrivick, J. L., Rowan, A. V., and James, M. R.:
1843 Quantifying ice cliff evolution with multi-temporal point clouds on the debris-covered Khumbu
1844 Glacier, Nepal, *J. Glaciol.*, 63, 823–837, <https://doi.org/10.1017/jog.2017.47>, 2017.
1845 Weidemann, S.S., Sauter, T., Malz, P., Jaña, R., Arigony-Neto, J., Casassa, G. and Schneider, C. (2018).
1846 Glacier Mass Changes of Lake-Terminating Grey and Tyndall Glaciers at the Southern Patagonia
1847 Icefield Derived From Geodetic Observations and Energy and Mass Balance Modeling. *Frontiers*
1848 *in Earth Science*, 6: 81. doi: 10.3389/feart.2018.00081.
1849 Wirbel, A., Jarosch, A. H., and Nicholson, L.: Modelling debris transport within glaciers by advection
1850 in a full-Stokes ice flow model, *The Cryosphere*, 12, 189–204, [https://doi.org/10.5194/tc-12-189-](https://doi.org/10.5194/tc-12-189-2018)
1851 [2018](https://doi.org/10.5194/tc-12-189-2018), 2018.
1852 Zekollari, H., Huss, M., Farinotti, D., and Lhermitte, S.: Ice-Dynamical Glacier Evolution Modeling—
1853 A Review, *Reviews of Geophysics*, 60, <https://doi.org/10.1029/2021RG000754>, 2022.
1854
1855

1856 **Tables and captions**

1857
1858
1859
1860
1861

Table 1. Regional Climate Models (RCMs) chosen for this study and details of the Global Circulation Models (GCMs) from which these are derived.

CORDEX South Asia regional climate model	Driving CMIP5 global climate model	CMIP5 modelling centre	RCM name in this study	Future precipitation scenario (qualitative)	2100 CE mean temperature change from present day (°C)	
					RCP 4.5	RCP 8.5
ITM-RegCM4	NOAA-GFDL-GFDL-ESM2M	National Oceanic and Atmospheric Administration (NOAA), USA	NOAA	Wet	1.4	3.8
ITM-RegCM4	CCCma-CanESM2	Canadian Centre for Climate Modelling and Analysis (CCCma), Canada	CCCma	Moderate	2.2	4.1
ITM-RegCM4	IPSL-CMSA-LR	Institut Pierre-Simon Laplace (IPSL), France	IPSL	Dry	1.6	3.8

Deleted: The NOAA RCM that was considered most representative of conditions in the Everest region. The temperature forcings used to project climate change beyond 2100 CE are global values (they are simply included against each of the RCMs for ease comparing with 2100 temperature change) and include no change in precipitation after 2100 CE.

Formatted Table

1862
1863
1864
1865
1866

Table 2: COSIPY model parameters, where α is albedo (of fresh snow, firm and ice), t^* decay time from snow to firm, d^* the constant for the effect of snow depth on albedo, and z_0 surface roughness length.

Parameter	Value	Unit	Source
$\alpha_{\text{freshsnow}}$	0.85	-	Mölg et al. 2012; Wagnon et al., 2009
α_{firm}	0.6	-	Knap and Oerlemans, 1996; Mölg et al. 2012
α_{ice}	0.3	-	Mölg et al. 2012
t^*	20	days	Mölg et al. 2012
d^*	1.0	cm	Mölg et al. 2012
$Z_{0\text{snow}}$	0.24	mm	Gromke et al., 2011
$Z_{0\text{firm}}$	4.0	mm	Brock et al., 2006
$Z_{0\text{ice}}$	1.7	mm	Brock et al., 2006
Z_0 ageing length (linearly from $Z_{0\text{snow}}$ to $Z_{0\text{firm}}$)	60	days	Mölg et al. 2012

Deleted: M

Deleted: The albedo values are widely used within the literature for clean. z_0 values are less well parameterised with high spatial variability across glacier surfaces. Testing revealed highest sensitivity of mass balance to $\alpha_{\text{freshsnow}}$ relative to the other parameters.

1867

1880
1881
1882

Figures and captions

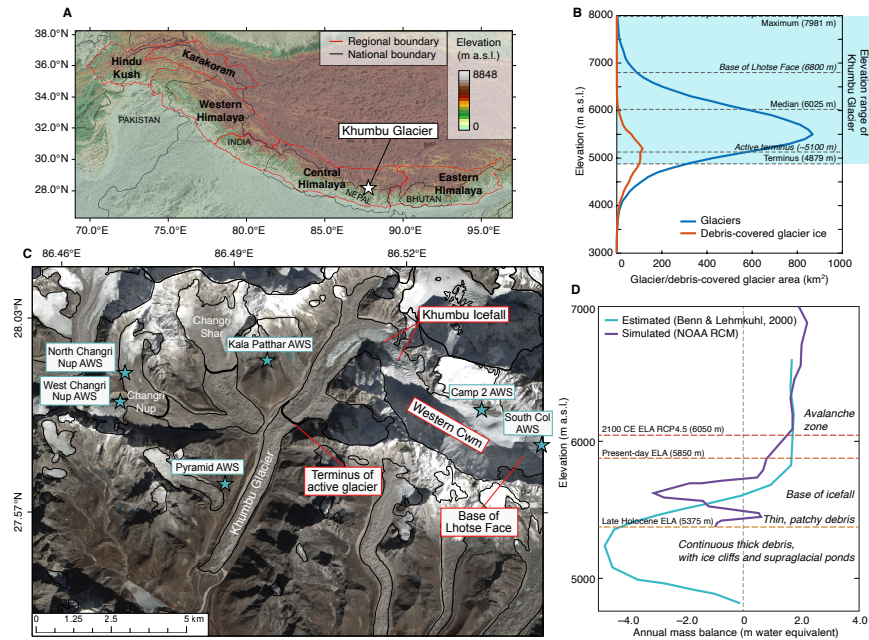
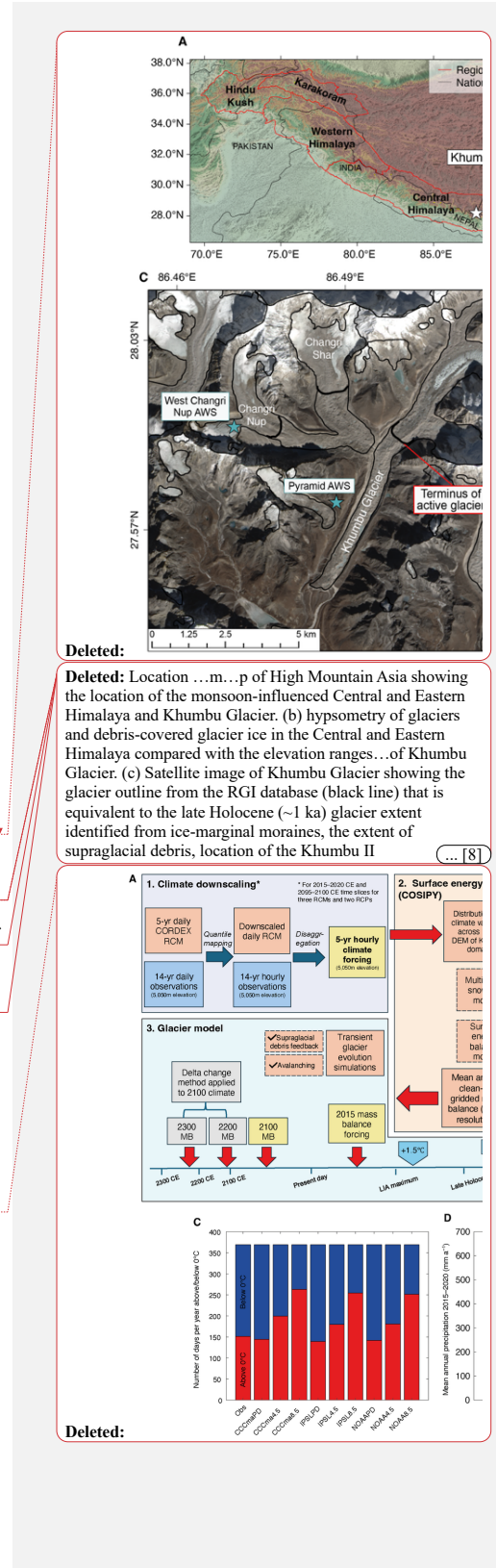
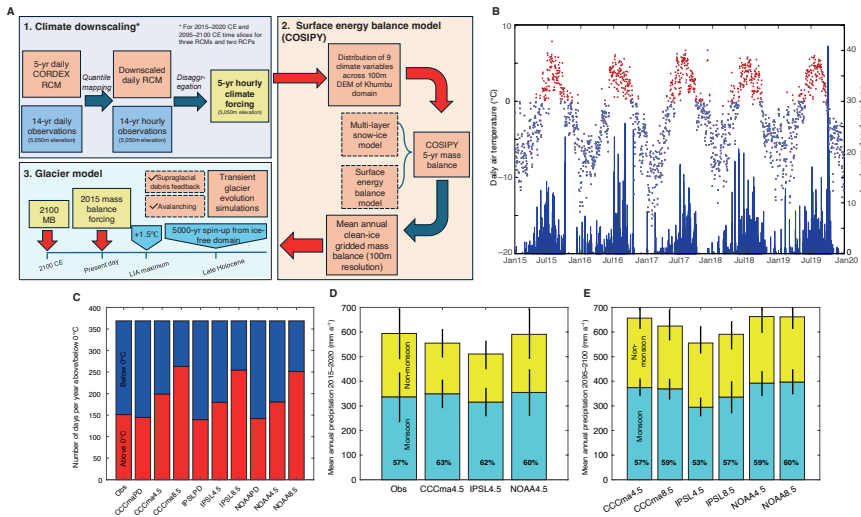


Figure 1: Khumbu Glacier location and context. (a) Map of High Mountain Asia showing the location of the monsoon-influenced Central and Eastern Himalaya and Khumbu Glacier. (b) hypsometry of glaciers and debris-covered glacier ice in the Central and Eastern Himalaya compared with the elevation range of Khumbu Glacier. (c) Satellite image of Khumbu Glacier showing the glacier outline from the RGI database (black line) that is equivalent to the late Holocene (~1 ka) glacier extent identified from ice-marginal moraines, the extent of supraglacial debris, location of the Khumbu Icefall, the extent of active ice flow inferred from observations of glacier velocity, and location of the automatic weather stations (AWS) used for RCM downscaling (blue stars). (d) Estimated mass balance gradient for debris-covered glaciers in the Everest region (Benn and Lehmkuhl, 2000) compared with the glacier mass balance gradient simulated using the NOAA RCM, and showing change in the equilibrium line altitude (ELA) of Khumbu Glacier in the historical and future simulations for the NOAA RCM RCP4.5 experiment.

1883
1884
1885
1886
1887
1888
1889
1890
1891
1892
1893
1894
1895
1896
1897
1898
1899
1900





1921
1922
1923
1924
1925
1926
1927
1928
1929
1930
1931
1932
1933
1934
1935
1936
1937
1938
1939
1940
1941
1942

Figure 2: Glacier model experimental design and evaluation of RCM downscaling. (a) Schematic diagram of the glacier modelling approach showing the methods used for downscaling through quantile mapping and disaggregation of climate data. Surface energy balance modelling using COSIPY includes the preprocessing stage of meteorological distribution across the Khumbu domain, which is repeated for each RCM in the 2015–2020 CE climates and for the three RCMs and two RCPs for the 2095–2100 CE climates. The simulated mass balances are then used to force the *SOSIA* model. (b) Daily mean temperature and daily total precipitation from the NOAA RCM for the present day (2015–2020 CE) following downscaling using quantile mapping with air temperature categorised into above freezing (red) and below freezing (blue). (c) Proportion of air temperatures above and below freezing for the present day for each RCM and RCP for the downscaled daily data compared with observations. (d) Annual precipitation totals for non-monsoon and monsoon months with standard deviation between selected years shown by black bars for the downscaled daily data compared with observations. (e) Future (2095–2100 CE) time-slice annual precipitation totals for non-monsoon and monsoon months with standard deviation between selected years shown by black bars. In (d) and (e) the percentage of the total annual precipitation occurring during the monsoon is indicated by the value in bold text. (Obs = meteorological observations from AWS).

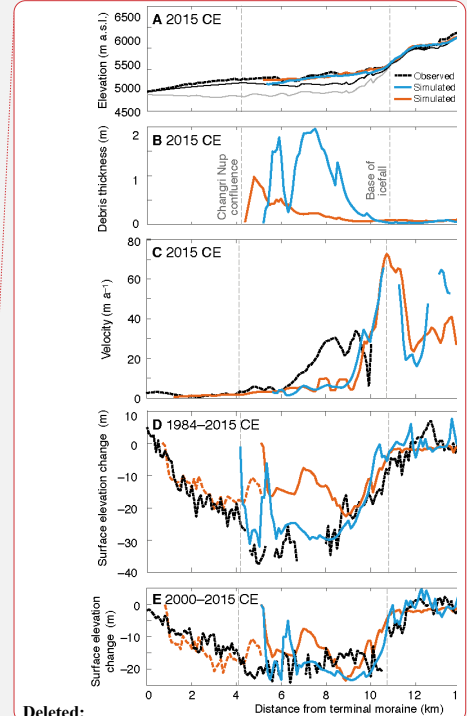
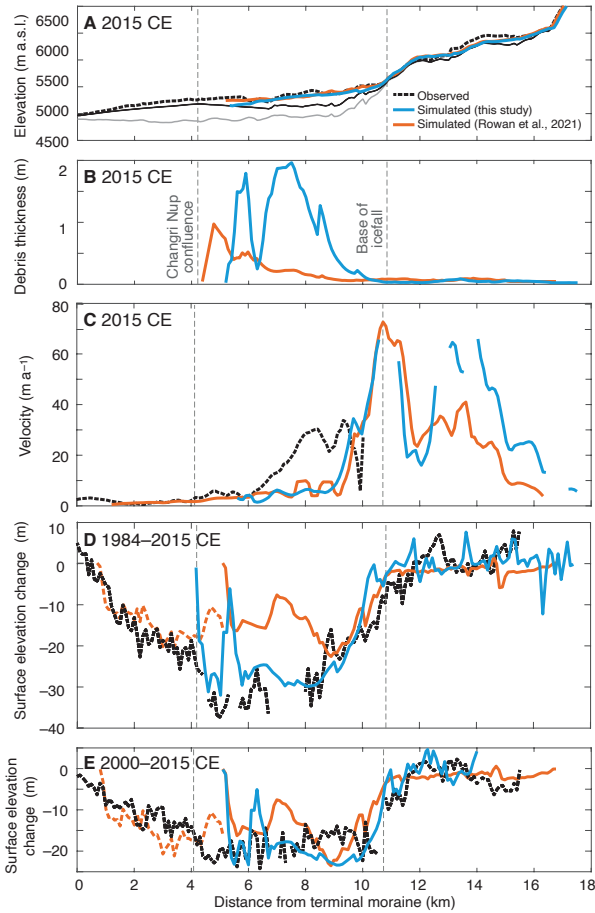
Deleted:

Deleted: Note that this process does not apply to the post-2100 CE climate forcings which are subject to delta change.

Deleted: -

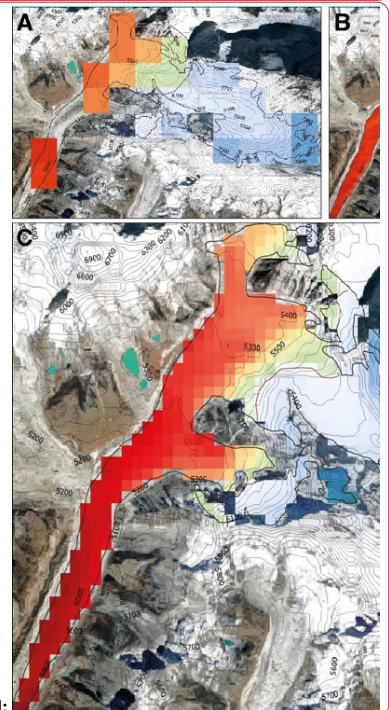
Deleted: is

Deleted: glacier evolution



Deleted:

Deleted:



Deleted:

1949
1950
1951
1952
1953
1954
1955
1956
1957
1958
1959
1960
1961
1962
1963
1964
1965
1966

Figure 3. Evaluation of present-day simulation showing; (a) mean simulated glacier surface elevation and bed elevation calculated from a 500 m-wide swath profile along the central flowline of the glacier. Subglacial topography including the dynamically detached debris-covered tongue is shown by the solid black line and subglacial topography used in the entire glacier simulations in Rowan et al. (2015) is shown for comparison by the lowermost grey solid line. The estimated present-day ice surface elevation (Farinotti et al., 2019) is shown by the dashed black line. (b) mean simulated debris thickness, (c) simulated and observed velocities from the NASA MEaSUREs ITS_LIVE project (Dehecq et al., 2019), and simulated and observed mean surface elevation change between (d) 1984–2015 CE and (e) 2000–2015 CE using geodetic observations from King et al. (2020) compared with results from the simulations in this study and those in Rowan et al. (2021), where further information about the model evaluation can be found.

1973
 1974
 1975
 1976
 1977
 1978
 1979
 1980
 1981
 1982
 1983
 1984

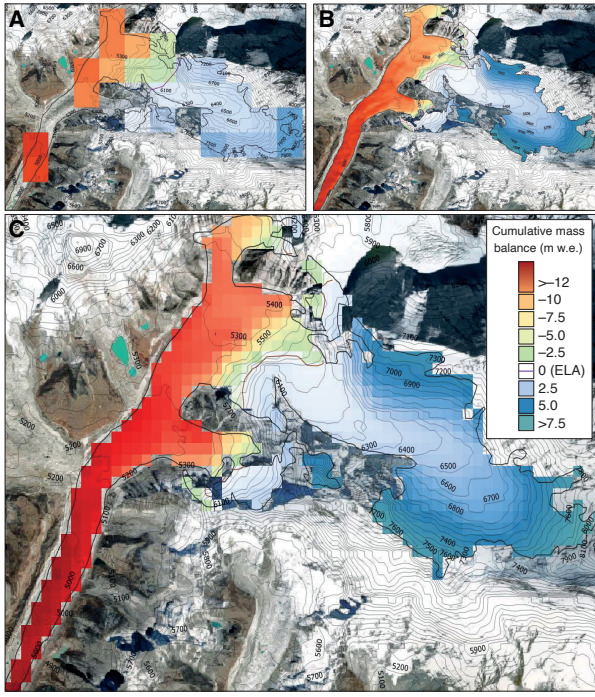


Figure 4. COSIPY reference calculation of present-day mass balance for Khumbu Glacier for the period 2013–2015 CE showing the results from calculations using different grid spacings using (a) a 1-km grid, (b) a 30-m grid, (c) the 200-m grid spacing used throughout the experiments in this study.

Formatted: Centred

Deleted: <object>

Deleted: <object><object><object>

Figure 5. Spatially averaged cumulative clean-ice mass balance with clear seasonality for (a) the present day time-slice including the mass balance forced by the observations used for downscaling, and the end-of-century time-slice under (b) RCP4.5 and (c) RCP8.5. The low annual glacier-wide mass balance values shown here are the result of the extent of the model domain used to force the glacier model that includes the larger catchment beyond the glacier margins and therefore contains a higher proportion of lower elevations than those of the glacier itself. However the similar mass balance results for simulations forced by NOAA RCM and observations can be clearly seen (a), and the differences between the three RCMs is apparent in all time-slices (a-c).

2001
2002
2003
2004
2005
2006
2007
2008
2009
2010
2011
2012

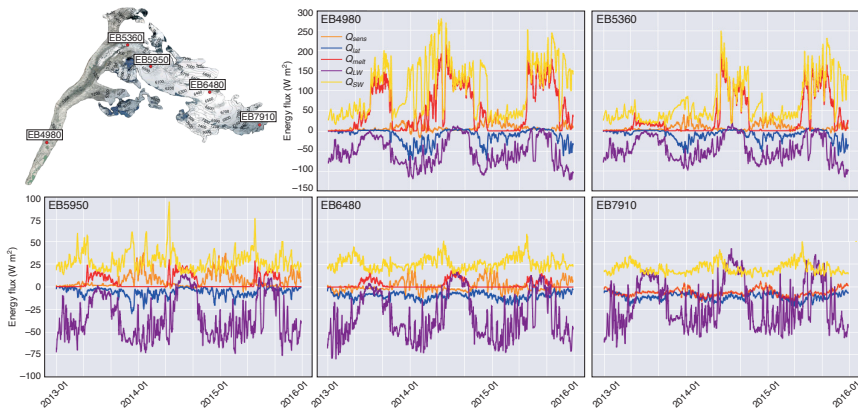


Figure 5. Locations of energy balance calculation points used for energy flux and melt components analysis in the reference calculation and sensitivity tests (named after their corresponding altitude e.g., EB6480) showing 5-day average of energy fluxes across study period for each site. Note that scales for energy flux are different for the two sites below the icefall compared to the three sites above the icefall.

2013
2014
2015
2016
2017
2018
2019
2020
2021
2022
2023

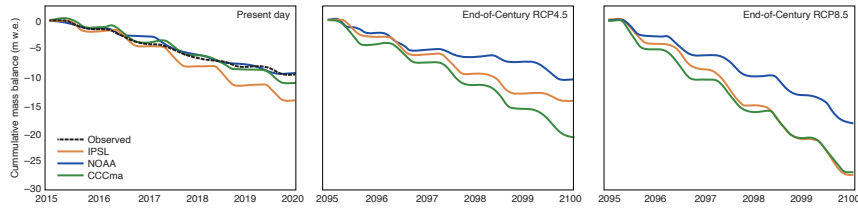


Figure 6. Spatially averaged cumulative clean-ice mass balance with clear seasonality for the present day time slice including the mass balance forced by the observations used for downscaling, and the end-of-Century time slice under RCP4.5 and RCP8.5. The low annual glacier-wide mass balance values shown here result from the extent of the model domain used to force the glacier model that includes the larger catchment beyond the glacier margins and therefore contains a higher proportion of lower elevations than those of the glacier itself. However the similarity between the mass balance results for simulations forced by NOAA RCM and observations can be clearly seen, and the differences between the three RCMs is apparent in all time slices.

Deleted:

Deleted: 6... (a) ...ocations of energy balance calculation (EB) ...oints used for energy flux and melt components analysis in the reference calculation and sensitivity tests (named after their corresponding altitude e.g., EB6480) and (b-f)...howing 5-day average of energy fluxes across study period for each site. Note that scales for energy flux are different for the two sites below the icefall (e) and (f) compared to (b)-(d)...he three sites above the icefall due to the marked difference in absolute values (... [9])

Calculated surface mass balance

Simulated glacier m...

NOAA present day conditions

Simulated glacier m...

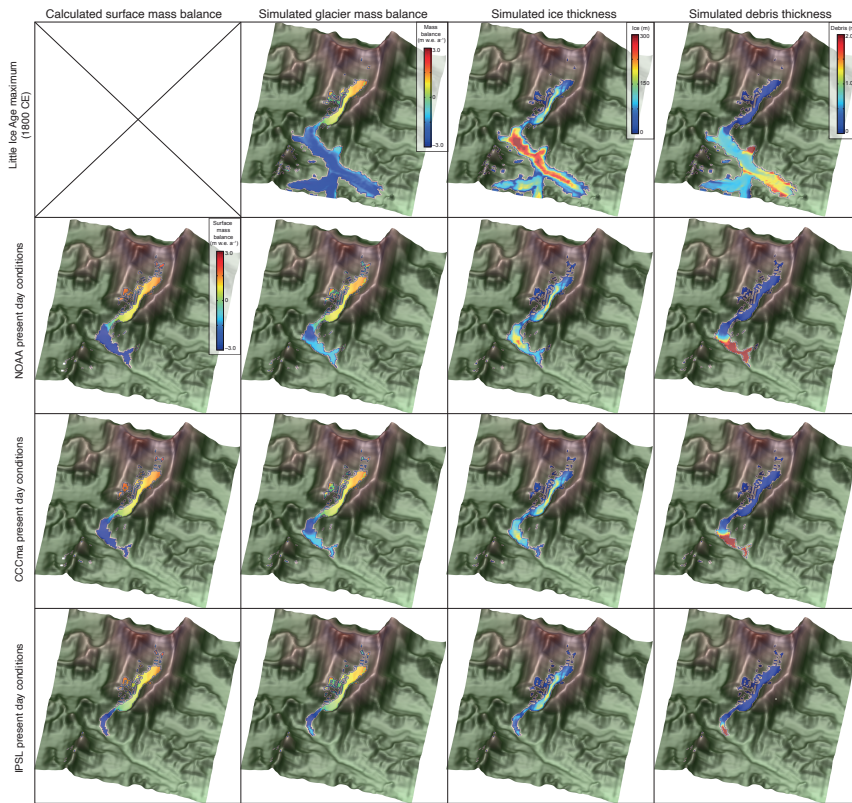
CCCma present day conditions

Simulated glacier m...

IPSL present day conditions

Simulated glacier m...

Deleted:

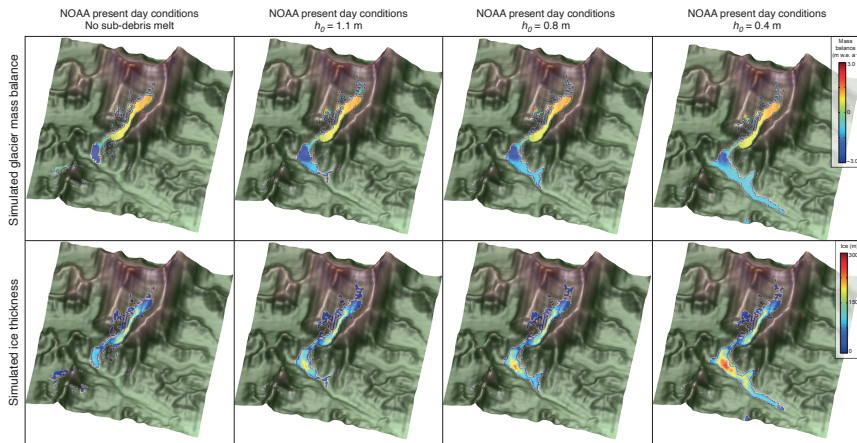


2047
2048
2049
2050
2051
2052
2053
2054
2055

Figure 7. **jSOSIA** model sensitivity to surface energy and mass balance forcing, showing 'Little Ice Age' (~1800 CE) **maximum** glacier mass balance, ice thickness and debris thickness. Present-day results for surface mass balance calculated using each RCM with COSIPY showing glacier mass balance calculated using the same climate forcing following integration with the glacier model, simulated ice thickness, and simulated debris thickness.

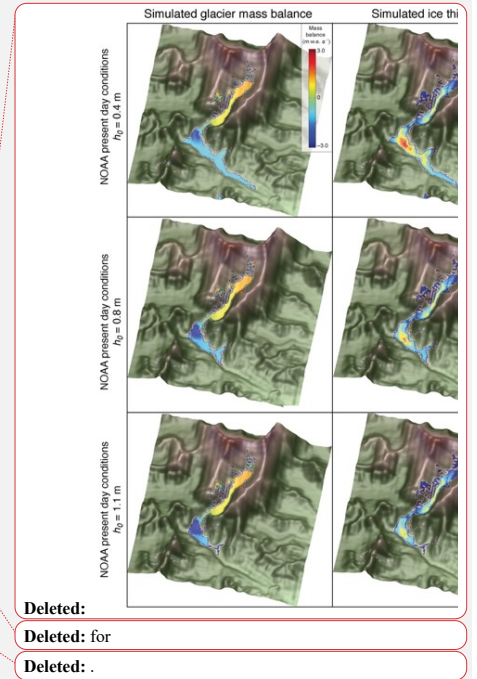
Deleted: Glacier

Formatted: Centred



2057
2058
2059
2060
2061
2062
2063
2064
2065
2066
2067

Figure 8. Glacier mass balance and ice thickness simulated using the NOAA RCM climate forcing and the resulting simulated ice thickness where no sub-debris melt is imposed and the glacier has an entirely debris-free surface compared with ice results for simulations with h_0 values of 0.4 m, 0.8 m, and 1.1 m where h_0 is a constant in Equation (1) representing the characteristic debris thickness at which the reduction in ablation due to insulation by supraglacial debris is 50% of the value for an equivalent clean-ice surface (Anderson and Anderson, 2016; Rowan et al., 2021).



2071
 2072
 2073
 2074
 2075
 2076
 2077
 2078
 2079
 2080
 2081
 2082

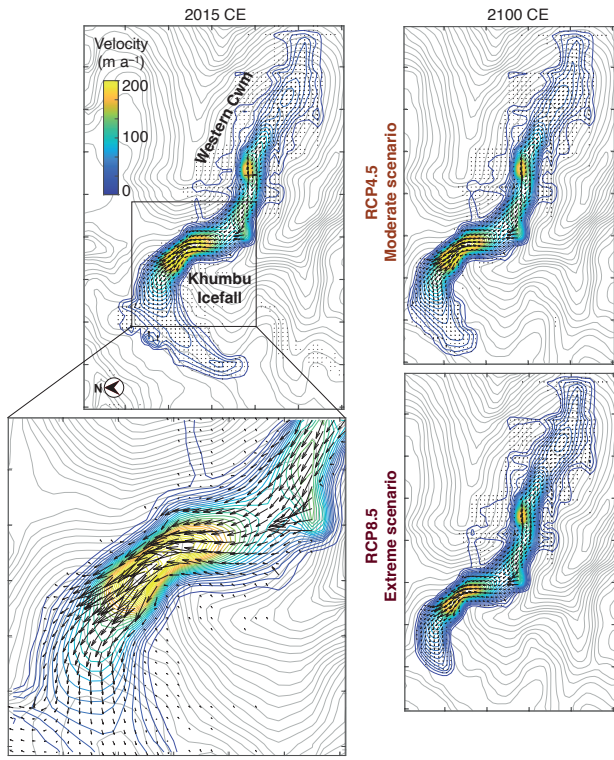
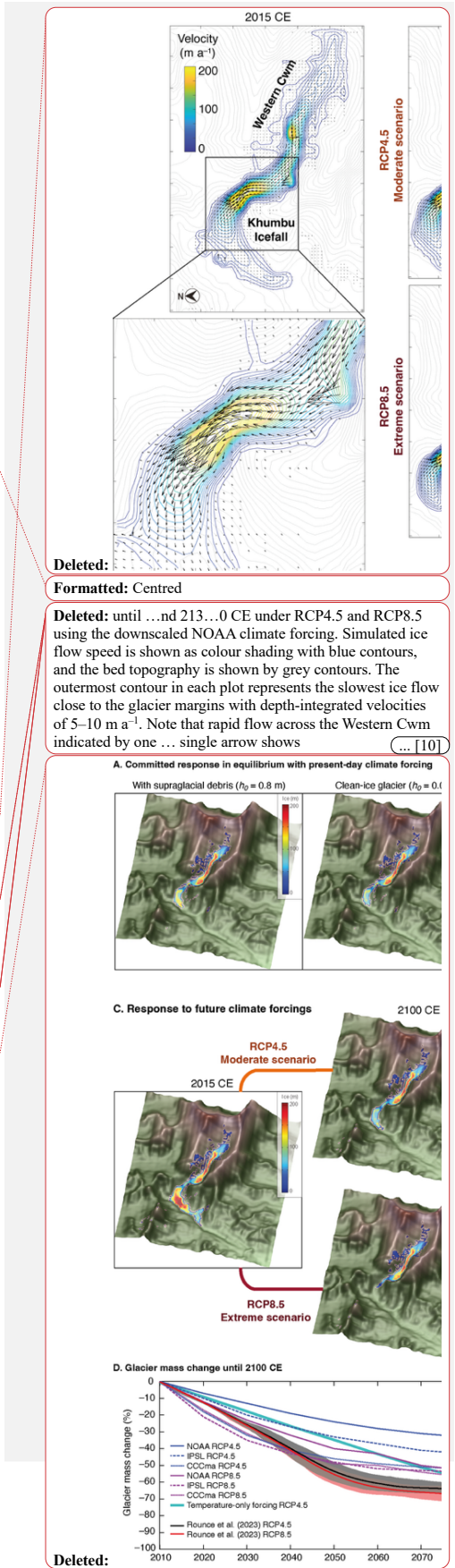
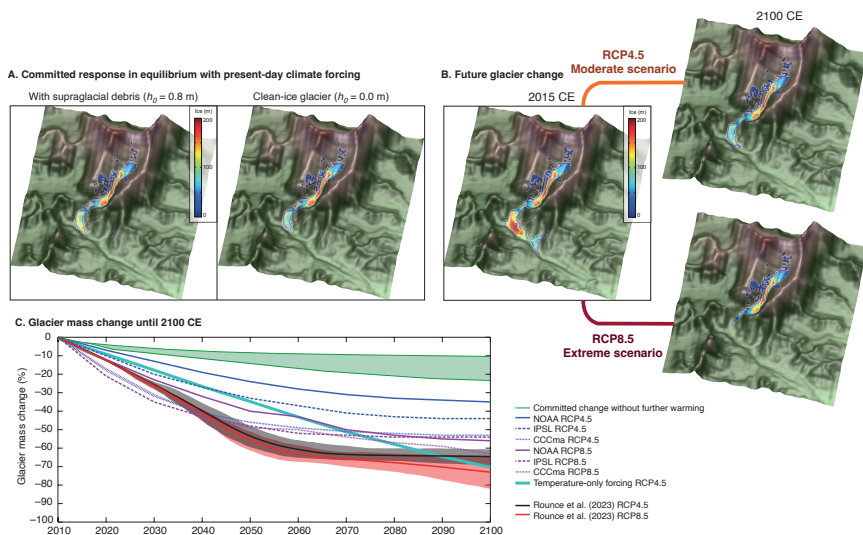


Figure 9. Simulated ice flow for Khumbu Glacier. Velocity-vector maps showing simulated ice flow magnitude and direction from the present day (2015–2020 CE) and 2100 CE under RCP4.5 and RCP8.5 using the downscaled NOAA climate forcing. Simulated ice flow speed is shown as colour shading with blue contours, and the bed topography is shown by grey contours. The outermost contour in each plot represents the slowest ice flow close to the glacier margins with depth-integrated velocities of 5–10 m a⁻¹. Note that rapid flow across the Western Cwm indicated by a single arrow represents the effects of avalanching rather than sustained glacier flow.





2106
2107
2108
2109
2110
2111
2112
2113
2114
2115
2116
2117
2118
2119

Figure 10. Future glacier volume change projections until 2100 CE. (a) Equilibrium ice thickness accounting for the committed response to recent climate change using the downscaled NOAA RCM climate forcing with and without the effect of supraglacial debris on mass balance. (b) Simulated ice thickness under RCP4.5 and RCP8.5 for 2100 CE using the downscaled NOAA RCM climate forcing. (c) Comparison of projected shrinkage of Khumbu Glacier by 2100 CE from this study with those from Rounce et al. (2023) showing results from each of the six experiments in this study with results from RCP4.5 and RCP8.5 from Rounce et al. (2023), the equivalent result for a simulation using a change in MAAT equivalent to the NOAA RCP4.5 forcing where precipitation does not change from the present-day value (cyan line). The green shading shows the range of the committed volume loss due to historical warming.

Deleted: (d) Comparison of projected shrinkage of Khumbu Glacier by 2100 CE from this study with those from Rounce et al. (2023) showing results from each of the six experiments in this study with results from RCP4.5 and RCP8.5 from Rounce et al. (2023), the equivalent result for a simulation using a change in MAAT equivalent to the NOAA RCP4.5 forcing where precipitation does not change from the present-day value (cyan line).
(b) Simulated glacier volume change from the present day (2015–2020 CE) until 2300 CE under RCP4.5 and RCP8.5 for the three downscaled RCMs. The black crosses mark when ice flow has declined sufficiently that the glacier is considered almost absent or no longer viable. The green shading shows the range of the committed volume loss due to historical warming.

Deleted: c

Deleted: ,

Deleted: 2200 CE and 2300 CE

Deleted: d

Deleted: ¶

Moved up [3]: (d) Comparison of projected shrinkage of Khumbu Glacier by 2100 CE from this study with those from Rounce et al. (2023) showing results from each of the six experiments in this study with results from RCP4.5 and RCP8.5 from Rounce et al. (2023), the equivalent result for a simulation using a change in MAAT equivalent to the NOAA RCP4.5 forcing where precipitation does not change from the present-day value (cyan line).

2148
2149
2150
2151
2152
2153
2154
2155
2156
2157
2158
2159
2160
2161
2162
2163
2164
2165
2166
2167
2168
2169
2170
2171
2172
2173
2174
2175
2176
2177
2178
2179
2180
2181
2182
2183
2184
2185
2186
2187
2188
2189
2190
2191
2192
2193
2194

Appendix

This appendix contains further details on the meteorological data collection and analysis, RCM downscaling, evaluation of the present-day downscaled RCM results using meteorological data and the distribution of these results across the model domain, and the parameterisation and sensitivity testing of the COSIPY model. The Indian Summer Monsoon season was defined as June to October, the post-monsoon as October–November, winter as December–February, and the pre-monsoon as March–May (Ueno et al., 2008). Although much of this study compares the monsoon season against the non-monsoon season, it should be noted that the timing of monsoon onset and cessation can vary between years. Day time was defined as 08:00–16:00 and night as 20:00–04:00 (Nepal local time) to account for changing sunrise and sunset times throughout the year and the influence of topographic shading in the valleys; centred-means were used for some datasets to remove local noise associated with daily frequencies. For sub-hourly measurements, hourly averages were calculated using data from the previous hour. The period for the reference simulation and sensitivity experiments was January 1st 2013 to December 31st 2015. RCM downscaling to produce the five-year time slices represented the periods January 1st 2015 to December 31st 2019 and January 1st 2095 to December 31st 2099.

A1. Gap filling of the AWS data

All AWS datasets contained periods of erroneous measurements and missing data, which is unsurprising given the challenges of maintaining equipment in such an environment (Oulkar et al., 2026). Daily air temperature averages were calculated when 83% (20 hours) of observations were available. For calculation of lapse rates for longer time periods (e.g. daytimes during the monsoon season) the distributions of missing data across these periods were analysed. For example, the Lukla AWS had almost 45% of temperature observations missing during the monsoon season but as these were equally distributed between day and night, lapse rates could be calculated using station pairs following the method of Immerzeel et al. (2014). Up to 13% of the West Changri Nup AWS temperature records were missing, and these were interpolated using the Ev-K2-CNR Pyramid AWS data with the same lapse rate as the GlacioClim dataset. The interpolated results were compared with the preceding and succeeding periods from the same AWS, and the preceding and succeeding months from other AWS, and compared with data collected in November 2014 at the GlacioClim North Changri Nup AWS (5,470 m a.s.l.).

Data gaps in the precipitation datasets were significant, particularly during the onset of the monsoon (e.g., 45% of data points were missing for the Namche AWS) meaning the altitudinal dependency of precipitation could not be fully characterised. This led to several monsoon seasons with little or no data at individual AWS. Given that the aim of this study was to analyse *in situ* trends, gap-filling through interpolation was not conducted for these AWS during the seasons without data. Station pairs were used to determine the elevation dependency of precipitation for the reference simulation following the method of Immerzeel et al. (2014). Results from the Kala Patthar/Pheriche station pair and the Pyramid/Pheriche station pair in 2009, and the Kala Patthar/Namche station pair during 2011, show that the relationship between precipitation amount and elevation was more negative during the monsoon season ($-0.011\% \text{ m}^{-1}$ to $-0.018\% \text{ m}^{-1}$) than during the non-monsoon ($-0.0039\% \text{ m}^{-1}$ to $-0.0043\% \text{ m}^{-1}$). No interpolation to fill data gaps was required for other meteorological variables, apart from albedo but as this was only measured at the West Changri Nup AWS there was no suitable surrogate for this variable.

A2. Downscaled climate model results compared with observations

Deleted: A: Climate Model Downscaling

Deleted: section

Deleted: ,

Moved down [4]: because this precipitation gauge provides a longer period of continuous observations than the other gauges and avoids errors due to low precipitation amounts measured by tipping bucket gauges, which are known to systematically underestimate snowfall particularly during high winds (Sherpa et al., 2017), because this precipitation

Moved (insertion) [4]

Deleted: ¶

A1. Meteorological data collection and analysis¶

14 years of meteorological observations were collected from two AWS at the Pyramid Observatory at 5,050 m a.s.l. and 5,035 m a.s.l. and the West Changri Nup Glacier AWS at 5,363 m a.s.l. Missing data were replaced through interpolation with an alternative AWS from this group. Precipitation was measured at 15-minute intervals using a Geonor T-200BM sensor mounted 1.8 m above the surface. Evaporation from the bucket is supposedly blocked by a layer of oil but some does occur as evidenced by precipitation values below 0 mm. Noise from wind and evaporation were corrected for by compensating any negative change over the 15-minute time step with the neighbouring positive value such that accumulated precipitation was unchanged. Periods with prolonged evaporation were set to zero. Undercatch of snowfall by rainfall gauges was corrected through precipitation phase partitioning using wind speed observations (Wagnon et al., 2009). For interpolation of air temperature, hourly lapse rates were used that averaged $5.54\text{ }^{\circ}\text{C km}^{-1}$ to adjust to the height of the reference point at 5,050 m a.s.l. Where possible, precipitation data taken from the Pyramid AWS at 5,035 m a.s.l. because this precipitation gauge provides a longer period of continuous observations than the other gauges and avoids errors due to low precipitation amounts measured by tipping bucket gauges, which are known to systematically underestimate snowfall particularly during high winds (Sherpa et al., 2017), because this precipitation gauge provides a longer period of continuous observations than the other gauges and avoids errors due to low precipitation amounts measured by tipping bucket gauges, which are known to systematically underestimate snowfall particularly during high winds (Sherpa et al., 2017)....

Formatted: Font: Bold

Formatted: Font: Bold

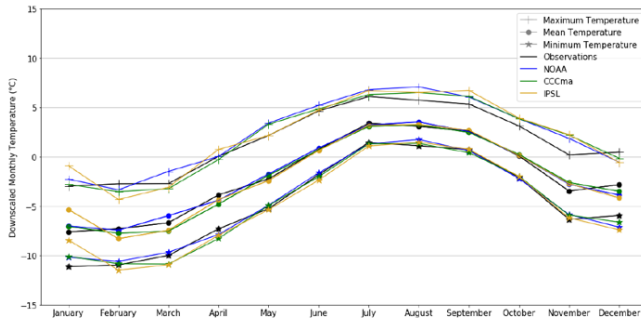
Formatted: Font: Bold

Formatted: Font: Italic

Deleted: ¶

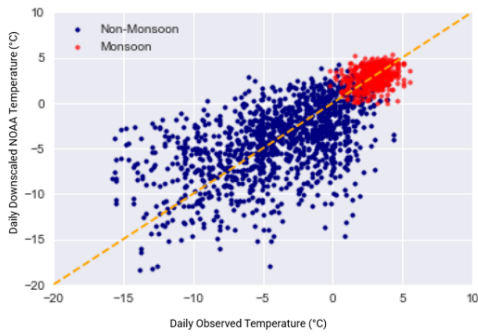
... [11]

Deleted: 1



2244
2245
2246
2247
2248
2249
2250
2251
2252

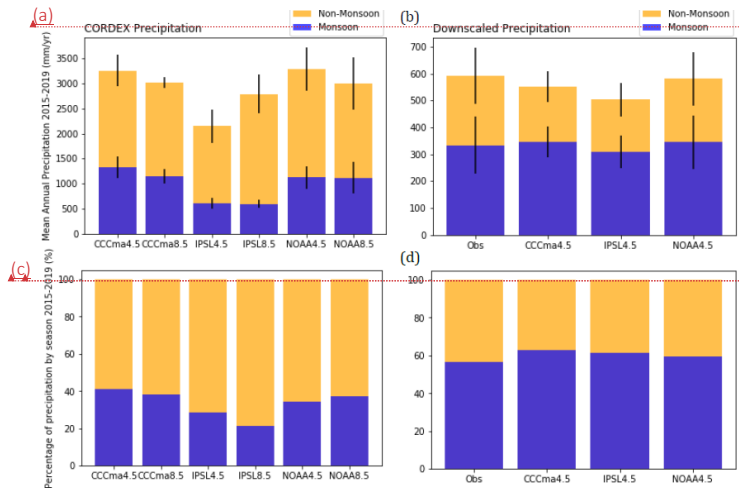
Figure A1: Downscaled monthly mean, maximum, and minimum temperature calculated for the present day time slice compared with observations from the GlacioClim Pyramid Observatory AWS.



2253
2254
2255
2256
2257
2258
2259
2260
2261

Figure A2: Daily downscaled temperature from the NOAA RCM against observations from the GlacioClim Pyramid Observatory AWS, split by monsoon/non-monsoon. The 1:1 relationship is shown by the dashed orange line.

- Deleted: ,
- Deleted: with a
- Deleted: line to aid analysis of the temperature distributions (
- Deleted:)



Formatted: Font: (Default) +Headings (Calibri Light), 10 pt

Formatted: Font: (Default) +Headings (Calibri Light), 10 pt

Formatted: Font: (Default) +Headings (Calibri Light), 10 pt

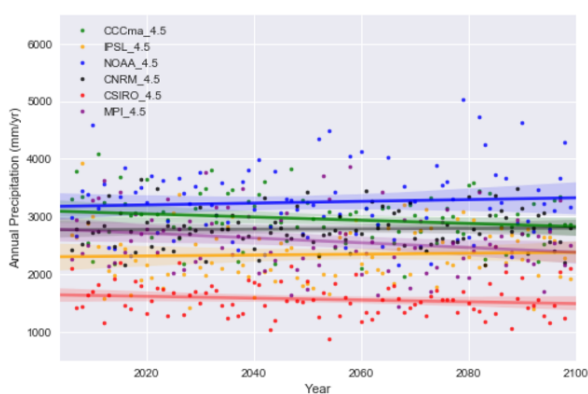
2266
2267
2268
2269
2270
2271
2272
2273
2274
2275
2276
2277
2278
2279
2280
2281

Figure A3. Annual precipitation totals for the monsoon and non-monsoon seasons, (a and b) Precipitation totals, before and after downscaling, with the standard deviation between selected years shown by black bars. (c and d) The same results as seasonal percentages. The annual precipitation is in good agreement with measurements in the southern Dudh Koshi catchment for the gridbox nearest to Khumbu Glacier is located at 27.9065056°N, 86.4352951°E at 2,100 m a.s.l..

- Deleted: for
- Deleted: non-monsoon and monsoon months
- Deleted: (a and b) and
- Deleted: their
- Deleted: (c and d)
- Deleted: matches
- Deleted: which is
- Deleted: 2
- Deleted: gure
- Deleted: i
- Deleted: d for

A3. Regional Climate Model analysis and selection

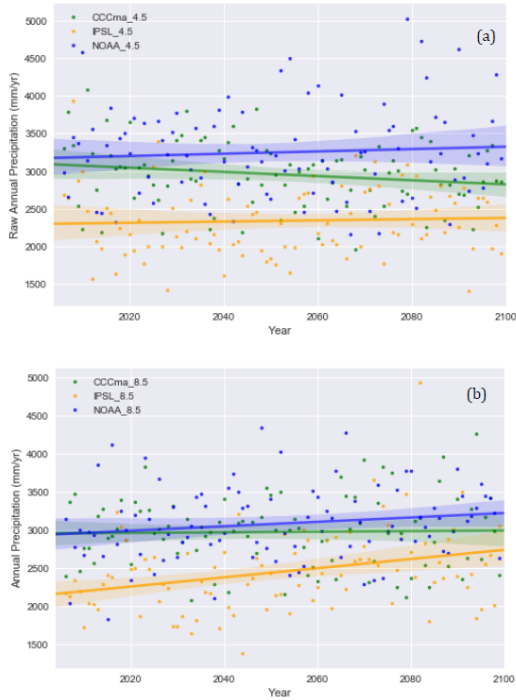
Three of the six available CORDEX South Asia RCMs (NOAA, CCCma, IPSL) were selected as discrete scenarios that spanned the range of possible future precipitation conditions (Table 1); either wet, moderate, or dry climate in 2080–2100 CE (Fig. A4). The raw RCMs significantly overestimated the annual total precipitation by at least a factor of five for the selected gridpoint, which was corrected by downscaling of these results using the AWS data.



2282
2283
2284
2285
2286

Figure A4: Annual precipitation sums (dots) with fitted trend line from the start of the RCP experiments (2006–2100 CE) for each of the six Indian Institute for Tropical Meteorology CORDEX models for RCP4.5.

- Deleted:) until the end (
- Deleted: ¶
- Deleted: ¶



2301
2302
2303
2304
2305
2306
2307
2308
2309
2310
2311
2312
2313
2314
2315
2316
2317

Figure A5: Annual precipitation sums (dots) with fitted trend line from the start of the RCP experiments (2006–2100 CE) for the three selected of the six CORDEX models for (a) RCP4.5 and (b) RCP8.5.

A.4. Downscaling parameters and method

While minimum and maximum air temperatures are not required to as inputs to COSIPY, these were downloaded and statistically downscaled using quantile mapping with normal distribution to aid disaggregation to an hourly time step using MELODIST (Table A1). Quantile mapping for the CORDEX wind speed data was found to be ineffective when analysing the time series output against observations, both for the absolute wind speed as well as the reduced day-on-day variability seen during the monsoon season, and therefore, GARD was used instead. This is a simple statistical analogue regression downscaling method appropriate for pointwise downscaling.

Table A1: RCM-derived parameters and the method used for downscaling or bias correction.

RCM-derived parameters	Downscaling/bias correction method	Parametric distribution model (for Quantile mapping)	References
Precipitation (kg per m ² per s, converted to mm day ⁻¹)	Quantile mapping	Gamma	Vrac et al., 2007; Piani et al., 2010
Mean temperature (K) Minimum temperature (K) Maximum temperature (K)	Quantile mapping	Normal / Gaussian	Li et al., 2010, Gupta et al., 2016; Luo et al., 2018
Incoming shortwave (W m ⁻²) Incoming longwave (W m ⁻²)	Quantile mapping	Beta	Ruane et al., 2015

- Formatted: Justified
- Deleted: (2006) until the end (2100)
- Deleted: (a)
- Deleted: (b)
- Deleted: ¶
- Formatted: Left
- Deleted: 3
- Deleted: Though
- Deleted: force
- Deleted: QM
- Deleted: . T

- Formatted: Font: Bold
- Deleted: QM
- Deleted: (QM)
- Deleted: QM
- Deleted: QM

Relative humidity (%)			
Pressure (hPa)	Bias correction	N/A	N/A
Wind speed (m s ⁻¹)	Regression downscaling	N/A	Gutmann et al., 2022

2331
2332
2333
2334
2335
2336
2337
2338
2339
2340
2341
2342
2343
2344
2345
2346
2347
2348
2349
2350
2351
2352
2353
2354
2355
2356

A5. Variability in surface energy balance with elevation

The contributions of the components of the surface energy balance were tested at five points along the glacier centreline (Fig. 5) and found to vary substantially in both absolute values and seasonality. Net shortwave radiation (Q_{SW}) contributed the largest energy input to the glacier surface at the lower elevation sites and correlated most strongly with Q_{melt} . The high temporal variability related to varied cloud cover and fluctuating albedo during the warmer months with the melting of the snowpack. Q_{SW} was low at higher elevations, but high SW_{in} at the higher sites indicates that this is not due to topographic shading. Q_{SW} is correlated with albedo, and the persistence of snow throughout much of the year will reduce Q_{melt} . Q_{LW} rose above zero during the monsoon season at sites EB5950, EB6480 and EB7910, mostly due to heavy cloud cover and increased temperatures relative to the glacier surface. Q_{net} was close to zero at the lower elevation sites as the arrival of the monsoon led to higher relative humidity, and this pattern was similar but dampened at higher elevations. At the highest site, EB7910, Q_{melt} correlated exactly with the sensible heat flux.

Sublimation occurred at all elevations, with the highest cumulative loss at EB7910 (Fig. A6A). Sublimation rates correlated with seasonality down-glacier; at EB7910 sublimation only slightly slowed from December until May, while sublimation at site EB4980 increased from April until the start of the monsoon in July. Subsurface melt at or above the ELA (5.950 m a.s.l.) was negligible, but lower elevation sites showed stronger seasonal cycles related to surface temperatures. Refreezing (Fig. A6C) occurred at all sites and the onset of refreezing was staggered with increasing elevation, although absolute values remained low. Higher Q_{in} during the monsoon resulted in higher deposition of snow to the glacier at lower elevations and negligible rates at higher elevations. Similar absolute values and patterns are seen for condensation (results not shown).

- Deleted: ¶
- Deleted: ¶ (... [12])
- Formatted: Font: Bold
- Formatted: Font: Bold
- Formatted: Font: Bold
- Formatted: Font: Italic
- Formatted: Font: Italic, Subscript
- Formatted: Font: Italic
- Formatted: Font: Italic, Subscript
- Formatted: Font: Italic
- Formatted: Font: Italic, Subscript
- Formatted: Font: Italic
- Formatted: Font: Italic, Subscript
- Formatted: Font: Italic, Subscript
- Formatted: Font: Italic
- Formatted: Font: Italic
- Formatted: Font: Italic, Subscript
- Formatted: Font: Italic
- Formatted: Font: Italic, Subscript
- Formatted: Font: Italic
- Formatted: Font: Italic, Subscript

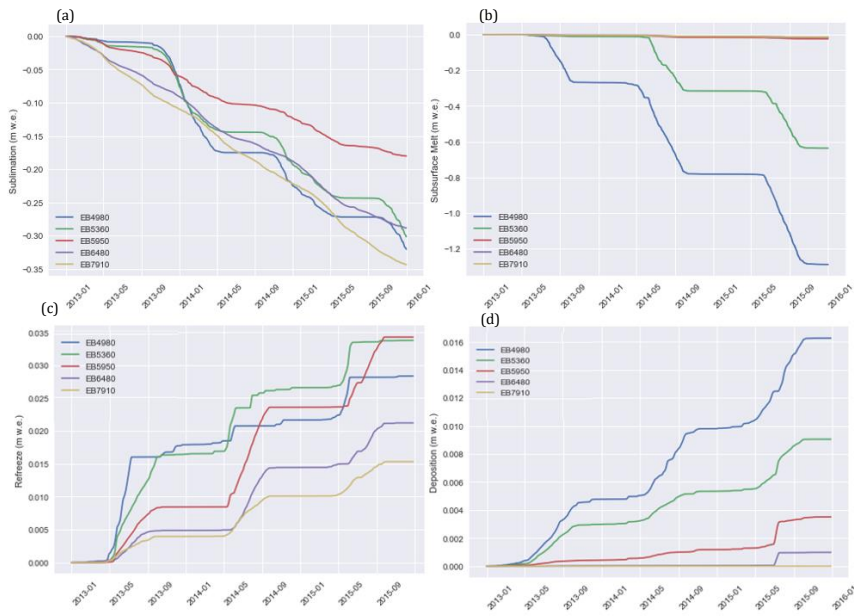


Figure A6. 5-day averages of (a) sublimation, (b) subsurface melt, (c) refreeze, and (d) deposition for the five surface energy balance sensitivity testing sites across Khumbu Glacier (see Fig. 5 for locations of these sites).

A6. COSIPY parameter testing and sensitivity results

To isolate the impact of individual surface energy balance variables on the mass balance of Khumbu Glacier, each variable was perturbed individually, and air temperature and precipitation amount were tested in tandem for the reference period 2013–2015 CE (Table A2). Perturbations of all variables were within the range of possible uncertainty that arise from a combination of observations, climate models, downscaling approach or the distribution of meteorology. The positive temperature and precipitation perturbations were in the order of possible future climate forcings. The spatially averaged mass balance was most sensitive to changes in LW_{in} , air temperature, and SW_{in} , and relative humidity had the least impact on ablation/accumulation rates (Fig. A7). The coupled parameter testing (Fig. A8) perturbed precipitation and air temperature simultaneously. The most significant change in spatially averaged mass balance followed a 3°C increase in air temperature and 20% decrease in precipitation amount. The increase in ablation following an increase in air temperature of 1.5°C was completely compensated by the increase in accumulation resulting from a 20% increase in precipitation amount.

Accurate estimation of precipitation phase is important for summer-accumulation type glaciers and threshold values of air temperature are often used to separate liquid and solid precipitation. Previous work calculated threshold temperatures across 6,883 AWS in the Northern Hemisphere to find an average rain/snow partitioning value of 1°C, with 95% of observations falling between 0.4°C and 2.4°C (Jennings et al., 2018). Although there remains a lack of such data for High Mountain Asia, Jennings et al. (2018) found that high mountain areas have the highest rain/snow partitioning thresholds, with a value of up to 4.5°C on the Tibetan Plateau. The impact of two different precipitation partitioning schemes on glacier mass balance was investigated here. Threshold temperatures of 0.5°C, 2.0°C and

Formatted: Font: Bold

Formatted: Font: Bold

Formatted: Font: Bold

2401 3.5°C were chosen and compared with the default value in COSIPY (STF), and a scheme that smoothly
 2402 scaled from 100% solid precipitation at -1°C to 0% solid precipitation at 4°C was also tested.

2403
 2404 The glacier ice surface roughness (z_0) was defined as 1.7 mm for the reference simulation, which is a
 2405 reasonable estimate for clean-ice glaciers (Mölg et al., 2012). The z_0 values reported within the literature
 2406 vary widely for clean-ice glaciers, and two substantially different z_0 values were tested. A z_0 value of
 2407 0.1 mm was measured at Midtre Lovénbreen, Svalbard (Irvine-Fynn et al. 2014), and August-One
 2408 glacier, China (Guo et al., 2018), and a z_0 value of 6.9 mm was calculated on the clean-ice section of
 2409 the Haut Glacier D’Arolla (Brock et al., 2006) and Laohugou Glacier No. 12 (Sun et al., 2018). These
 2410 values were used as endmembers of the likely range in values for Khumbu Glacier. The z_0 value had
 2411 minimal impact on glacier mass balance (Fig. A9) although a higher (lower) value for z_0 did result in
 2412 slightly increased (decreased) mass balance. The mass balance sensitivity was not proportional to the
 2413 change in z_0 , with a z_0 value of 1.6 mm lower than the reference value leading to a similar mass balance
 2414 change than that of the experiment with a z_0 value of 5.2 mm higher than the reference value.

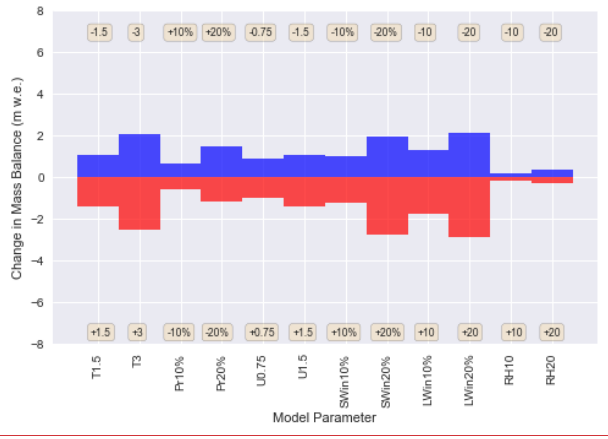
2415
 2416 The albedo values of the three glacier components were perturbed by ± 0.05 from that used in the
 2417 reference experiment (e.g., 0.85 for fresh snow). There was a strong response of the glacier mass balance
 2418 to changing snow albedo. Reducing snow albedo by 0.05 led to a 65% reduction in mass balance of
 2419 2.21 m w.e. (Fig. A9). Ablation (accumulation) rates were 3.7 m w.e. (1.75 m w.e.) higher relative to
 2420 the reference simulation for this perturbation. This result further supports the importance of Q_{SW} to
 2421 ablation rates. Varying albedo values for firn and ice also revealed a lower sensitivity of glacier mass
 2422 balance relative to snow albedo.

2423
 2424
 2425 Table A2. Parameter perturbations for the sensitivity experiments. Note that for relative humidity the %
 2426 refers to the units and not the perturbation.

Parameter	Perturbation
Mean annual air temperature (C)	$\pm 1.5, \pm 2.0, \pm 3.0$
Precipitation amount (%)	$\pm 10, \pm 20, \pm 30$
Wind speed ($m s^{-1}$)	$\pm 0.75, \pm 1.5$
SW_{in} and LW_{in} (%)	$\pm 10, \pm 20$
Relative Humidity (%)	$\pm 10, \pm 20$

- Formatted: Font: Bold
- Formatted Table
- Formatted: Superscript
- Formatted: Subscript
- Formatted: Subscript
- Formatted: Centred

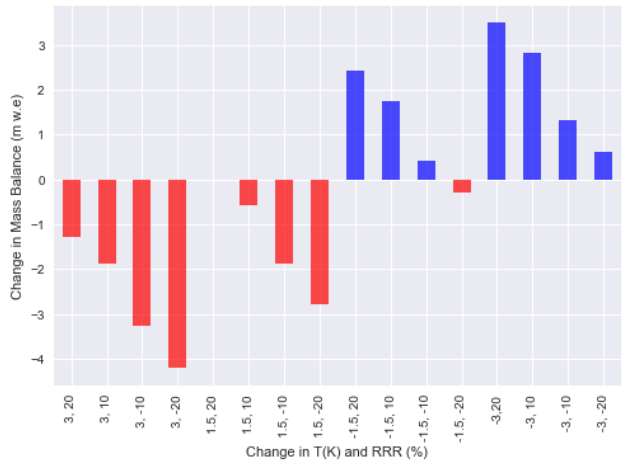
2428



2429
 2430
 2431 Figure A7. Single parameter sensitivity test results for reference simulation period 2013–2015 CE.

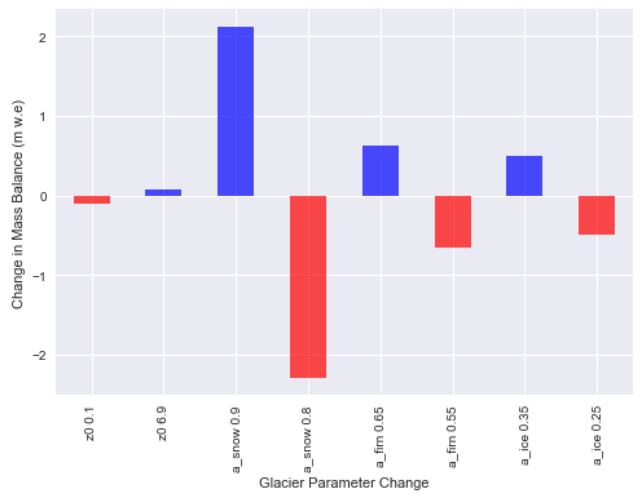
- Formatted: Left

2432
 2433
 2434
 2435
 2436
 2437
 2438



Formatted: Centred

2439
 2440
 2441
 2442
 2443
 2444
 2445
 2446
 2447
 2448



Formatted: Centred

2449 **Additional references for Appendix A**

- 2450 Gupta, A. and Tarboton, D.G. 2016. A tool for downscaling weather data from large-grid reanalysis
2451 products to finer spatial scales for distributed hydrological applications. *Environmental*
2452 *Modelling & Software*, 84, pp. 50–69. <https://doi.org/10.1016/j.envsoft.2016.06.014>
- 2453 Gutmann, E. D., J. J. Hamman, M. P. Clark, T. Eidhammer, A. W. Wood, and J. R. Arnold, 2022: En-
2454 GARD: A Statistical Downscaling Framework to Produce and Test Large Ensembles of Climate
2455 Projections. *J. Hydrometeorol.*, 23, 13545–1561, <https://doi.org/10.1175/JHM-D-21-0142.1>.
- 2456 Immerzeel, W., Petersen, L., Ragetti, S. and Pellicciotti, F. 2014. The importance of observed gradients
2457 of air temperature and precipitation for modelling runoff from a glacierized watershed in the
2458 Nepalese Himalayas. *Water Resources Research*. 50: 2212-2226. doi: 10.1002/2013WR014506.
- 2459 [Jennings, K. S., Winchell, T. S., Livneh, B., and Molotch, N. P.: Spatial variation of the rain-snow](https://doi.org/10.1038/s41467-018-03629-7)
2460 [temperature threshold across the Northern Hemisphere, *Nat Commun.*, 9, 1148,](https://doi.org/10.1038/s41467-018-03629-7)
2461 <https://doi.org/10.1038/s41467-018-03629-7>, 2018.
- 2462 Lente, G. and Ósz, K., 2020. Barometric formulas: various derivations and comparisons to
2463 environmentally relevant observations. *ChemTexts*, 6, pp.1-14. [https://doi.org/10.1007/s40828-](https://doi.org/10.1007/s40828-020-0111-6)
2464 [020-0111-6](https://doi.org/10.1007/s40828-020-0111-6)
- 2465 Li, H., Sheffield, J. and Wood, E.F., 2010. Bias correction of monthly precipitation and temperature
2466 fields from Intergovernmental Panel on Climate Change AR4 models using equidistant quantile
2467 matching. *Journal of Geophysical Research: Atmospheres*, 115(D10),
2468 <https://doi.org/10.1029/2009JD012882>
- 2469 [Oulkar, S. N., Peacey, M. W., Mitrev, M., Quincey, D. J., Hubbard, B., Matthews, T., Oulkar, A. S.,](https://doi.org/10.5194/gi-15-75-2026.2026)
2470 [Miles, K. E., and Rowan, A. V.: Design and implementation of a robust data logging and satellite](https://doi.org/10.5194/gi-15-75-2026.2026)
2471 [telemetry system for remote cryospheric research, *Geosci. Instrum. Method. Data Syst.*, 15, 75–](https://doi.org/10.5194/gi-15-75-2026.2026)
2472 [88, https://doi.org/10.5194/gi-15-75-2026.2026.](https://doi.org/10.5194/gi-15-75-2026.2026)
- 2473 Ruane, A. C., Goldberg, R., and Chrysanthacopoulos, J. 2015. Climate forcing datasets for agricultural
2474 modeling: Merged products for gap-filling and historical climate series estimation, *Agricultural*
2475 *and Forest Meteorology*, 200, pp. 233–248. <https://doi.org/10.1016/j.agrformet.2014.09.016>
- 2476 Salerno, F., Guyennon, N., Thakuri, S., Viviano, G., Romano, E., Vuillermoz, E., Cristofanelli, P.,
2477 Stocchi, P., Agrillo, G., Ma, Y., and Tartari, G. (2015). Weak precipitation, warm winters and
2478 springs impact glaciers of south slopes of Mt. Everest (central Himalaya) in the last 2 decades
2479 (1994–2013), *The Cryosphere*. 9: 1229-1247. doi: 10.5194/tc-9-1229-2015.
- 2480 [Sun, W., Qin, X., Wang, Y. et al. The response of surface mass and energy balance of a continental](https://doi.org/10.1007/s00382-017-3823-6)
2481 [glacier to climate variability, western Qilian Mountains, *China. Clim Dyn* 50, 3557–3570 \(2018\).](https://doi.org/10.1007/s00382-017-3823-6)
2482 <https://doi.org/10.1007/s00382-017-3823-6>
- 2483 Vrac, M., Stein, M.L., Hayhoe, K. and Liang, X.Z., 2007. A general method for validating statistical
2484 downscaling methods under future climate change. *Geophysical Research Letters*, 34(18),
2485 <https://doi.org/10.1029/2007GL030295>
- 2486 Wohlfahrt, G., Hammerle, A., Haslwanter, A., Bahn, M., Tappeiner, U. and Cernusca, A. 2008.
2487 Disentangling leaf area and environmental effects on the response of the Net Ecosystem Co2
2488 Exchange to diffuse radiation, *Geophysical Research Letters*, 35(16),
2489 doi:10.1029/2008gl035090.
- 2490 Wohlfahrt, G., Hammerle, A., Niedrist, G., Scholz, K., Tomelleri, E. and Zhao, P. 2016. On the energy
2491 balance closure and net radiation in complex terrain, *Agricultural and Forest Meteorology*, 226–
2492 227, pp. 37–49. doi:10.1016/j.agrformet.2016.05.012.
- 2493 Yang, K., N. Guyennon, L. Ouyang, L. Tian, G. Tartari, and F. Salerno (2017). Impact of summer
2494 monsoon on the elevation-dependence of meteorological variables in the south of Central
2495 Himalaya. *International Journal of Climatology*. 5293: 1748-1759. doi:10.1002/joc.5293.

Page 3: [1] Deleted	Ann Rowan	26/02/2026 11:07:00
Page 3: [2] Deleted	Ann Rowan	05/03/2026 13:21:00
Page 3: [3] Deleted	Ann Rowan	06/03/2026 08:53:00
Page 4: [4] Deleted	Ann Rowan	06/03/2026 09:04:00
Page 10: [5] Deleted	Ann Rowan	06/03/2026 12:50:00
Page 12: [6] Deleted	Ann Rowan	26/02/2026 11:00:00
Page 14: [7] Deleted	Ann Rowan	06/03/2026 13:33:00
Page 25: [8] Deleted	Ann Rowan	26/02/2026 14:23:00
Page 25: [8] Deleted	Ann Rowan	26/02/2026 14:23:00
Page 25: [8] Deleted	Ann Rowan	26/02/2026 14:23:00
Page 25: [8] Deleted	Ann Rowan	26/02/2026 14:23:00
Page 29: [9] Deleted	Ann Rowan	06/03/2026 12:29:00
Page 29: [9] Deleted	Ann Rowan	06/03/2026 12:29:00
Page 29: [9] Deleted	Ann Rowan	06/03/2026 12:29:00
Page 29: [9] Deleted	Ann Rowan	06/03/2026 12:29:00
Page 29: [9] Deleted	Ann Rowan	06/03/2026 12:29:00
Page 29: [9] Deleted	Ann Rowan	06/03/2026 12:29:00
Page 29: [9] Deleted	Ann Rowan	06/03/2026 12:29:00
Page 29: [9] Deleted	Ann Rowan	06/03/2026 12:29:00
Page 29: [9] Deleted	Ann Rowan	06/03/2026 12:29:00
Page 32: [10] Deleted	Ann Rowan	26/02/2026 14:32:00
Page 32: [10] Deleted	Ann Rowan	26/02/2026 14:32:00
Page 32: [10] Deleted	Ann Rowan	26/02/2026 14:32:00
Page 32: [10] Deleted	Ann Rowan	26/02/2026 14:32:00
Page 34: [11] Deleted	Ann Rowan	05/03/2026 10:44:00

